ISSN 8755-6839

SCIENCE OF **TSUNAMI HAZARDS**

Journal of Tsunami Society International

Volume 35 **Number 2** **2016**

TSUNAMI SOCIETY INTERNATIONAL, 1741 Ala Moana Blvd. #70, Honolulu, HI 96815, USA.

SCIENCE OF TSUNAMI HAZARDS is a CERTIFIED OPEN ACCESS Journal included in the prestigious international academic journal database DOAJ, maintained by the University of Lund in Sweden with the support of the European Union. SCIENCE OF TSUNAMI HAZARDS is also preserved, archived and disseminated by the National Library, The Hague, NETHERLANDS, the Library of Congress, Washington D.C., USA, the Electronic Library of Los Alamos, National Laboratory, New Mexico, USA, the EBSCO Publishing databases and ELSEVIER Publishing in Amsterdam. The vast dissemination gives the journal additional global exposure and readership in 90% of the academic institutions worldwide, including nation-wide access to databases in more than 70 countries.

OBJECTIVE: Tsunami Society International publishes this interdisciplinary journal to increase and disseminate knowledge about tsunamis and their hazards.

DISCLAIMER: Although the articles in SCIENCE OF TSUNAMI HAZARDS have been technically reviewed by peers, Tsunami Society International is not responsible for the veracity of any statement, opinion or consequences.

Submit manuscripts of research papers, notes or letters to the Editor. If a research paper is accepted for publication the author(s) must submit a scan-ready manuscript, a Doc, TeX or a PDF file in the journal format. Issues of the journal are published electronically in PDF format. There is a minimal publication fee for authors who are members of Tsunami Society International for three years and slightly higher for non-members. Tsunami Society International members are notified by e-mail when a new issue is available. Permission to use figures, tables and brief excerpts from this journal in scientific and educational works is granted provided that the source is acknowledged.

Recent and all past journal issues are available at: http://www.TsunamiSociety.org CD-ROMs of past volumes may be purchased by contacting Tsunami Society International at postmaster@tsunamisociety.org Issues of the journal from 1982 thru 2005 are also available in PDF format at the U.S. Los Alamos National Laboratory Library http://epubs.lanl.gov/tsunami/

ISSN 8755-6839

SCIENCE OF **TSUNAMI HAZARDS**

Journal of Tsunami Society International

Volume 35 **Number 2** **2016**

BENCHMARK SOLUTIONS FOR TSUNAMI WAVE FRONTS AND RAYS. PART 1: SLOPING BOTTOM TOPOGRAPHY

Andrey G. Marchuk

Institute of Computational Mathematics and Mathematical Geophysics, Novosibirsk, Russia

ABSTRACT

In this paper, the kinematics of tsunami wave rays and fronts over an uneven bottom are studied. A formula for the wave height along a ray tube is obtained. An exact analytical solution for wave rays and fronts over a sloping bottom is derived. This solution makes possible to determine a tsunami wave height in an area with a sloping bottom from the initial source in the ray approximation. The distribution of wave-height maxima calculated in an area with a sloping bottom is compared to that obtained with a shallow-water model.

Keywords: *tsunami, wave kinematics, wave ray and front, exact solutions for sloping bottom*

Vol. 35, No. 2, Page 34, (2016)

1. SOME FEATURES OF THE LONG WAVE PROPAGATION

Tsunami waves usually generated by vertical displacements of large ocean bottom areas belong to a class of long waves whose length is at least ten times greater than the depth. The propagation of such waves in a deep ocean, where the wave height is usually two orders smaller than the depth, is described by a linear system of differential shallow-water equations (Stocker, 1957). The validity of this description has many times been verified in practice. In the one-dimensional case without external forces (except for the gravity) these equations can be written down in the following form:

$$\frac{\partial u}{\partial t} + g\frac{\partial \eta}{\partial x} = 0 \tag{1.1}$$

$$\frac{\partial \eta}{\partial t} + \frac{\partial (Du)}{\partial x} = 0 \tag{1.2}$$

Here u is the horizontal water flow velocity in the wave, η is the water surface height above an unperturbed level, g is the acceleration of gravity, and D is the depth. It follows from the shallow-water equations that the wave velocity does not depend on its length, and is determined by the Lagrange formula (Stocker, 1957):

$$c = \sqrt{gD} \tag{1.3}$$

This formula is of fundamental importance for the kinematics of long waves (in particular, tsunamis). The wave front may be defined as interface between the undisturbed water (the height η and velocity components are zero) and the water area, where the perturbation from the source has already arrived at the time instant ($\eta \neq 0$). To describe the tsunami wave dynamics in the coastal zone where the tsunami amplitude increases and the depth decreases, we use the nonlinear shallow water model (Marchuk et al, 1983) in which the wave propagation velocity is expressed by the formula

$$c = \sqrt{g(D+\eta)} \tag{1.4}$$

Let us note that the front and wave crest velocities are somewhat different. However, the crest, where the water surface height reaches a maximum along the entire wavelength, gradually catches up with the front. When the crest passes the front, the wave breaks. If a wave propagates in a deep ocean this effect is weak even if it passes the entire water area of the Pacific Ocean. In what follows, when considering the kinematics of long wave propagation velocity means wave front velocity, which, according to (1.3), does not depend on the wave parameters and is solely defined by the ocean depth at the place, where the wave currently is. The fact that the front propagation velocity of a tsunami wave does not depend on its amplitude and length is determinative for behavior of such waves in water areas with an uneven bottom.

The properties of the system of shallow water equations and peculiarities of the physical process of tsunami wave propagation make possible to obtain estimates for the parameters of the flow in this wave that can be used to determine the tsunami height. Specifically, the fact that the horizontal velocity in the long wave motion is constant in the entire bulk of water (from surface to bottom) is taken into account (Stocker, 1957). All relations to be obtained in this Section are valid for the linearized shallow water equations. These relations are also accurate up to second order for tsunami propagation described by the nonlinear shallow water equations in the deep ocean, where the depth is two orders greater than the wave amplitude. First let us obtain an approximate formula for the horizontal flow velocity u in a moving tsunami wave if the depth is equal to D. Such a relation can be explicitly obtained from the linearized shallow water equations (1.1) and (1.2). We know that in this model the wave velocity is determined by the Lagrange formula (1.3). Let a running wave be represented as a harmonic function

$$\eta = a\cos(kx - \omega t), \tag{1.5}$$

which describes a wave of height a running in the direction of increasing the coordinate x with the velocity $c = \omega/k$. Substituting the expression for water surface displacement (1.5) into equation (1.1), we have

$$\frac{\partial u}{\partial t} = gka\sin(kx - \omega t). \tag{1.6}$$

Integrating both sides of (1.6) with respect to t, we obtain the following relation between the flow velocity in the wave and its amplitude and depth:

$$u = \int \frac{gk}{\omega} a\sin(kx - \omega t)d(kx - \omega t) = \frac{g}{c}(a\cos(kx - \omega t)) = \frac{g}{\sqrt{gD}}\eta = \eta\sqrt{\frac{g}{D}}. \tag{1.7}$$

Thus, in a harmonic wave of the form of (1.5) the water flow velocity is defined by formula (1.7). However, since the process is linear, formula (1.7) will be valid for any long wave that can be represented as superposition of harmonic waves with different frequencies and is a solution to the system of linear differential shallow water equations (1.1) and (1.2). For the quasilinear system of shallow water equations, where the wave front and crest velocities are somewhat different and determined by (1.4), the horizontal flow velocity in a moving wave has the form

$$u = \eta\sqrt{\frac{g}{D + \eta}}, \tag{1.8}$$

where η is the wave height, D is the depth, and g is the acceleration of gravity. An expression for the kinetic energy of a propagating one-dimensional tsunami wave with allowance for formula (1.8) is as follows:

$$E_K = \int_0^L \frac{\rho u^2}{2}(D+\eta)dx = \int_0^L \frac{\rho \eta^2}{2}\frac{g}{(D+\eta)}(D+\eta)dx = \int_0^L \frac{\rho \eta^2 g}{2}dx \quad , \tag{1.9}$$

where L is the wavelength, and ρ is the liquid density. Let us also write down an expression for the potential energy assuming that the potential energy of a quiet liquid is zero,

$$E_P = \int_0^L \frac{\rho g \eta^2}{2}dx \tag{1.10}$$

A comparison of the integrands in the formulas for the kinetic and the potential energies of a running tsunami wave show their identical equality. Hence, in any segment of the wave the kinetic energy is equal to the potential energy.

Now, using formula (1.7), we can find an approximate relation between the height of a plane (one-dimensional) tsunami wave and depth. Let at a point $x = x_1$ the depth be equal to D_1 and the mareogram (the ocean surface elevation versus time) of a one-dimensional tsunami wave be expressed by the function $\eta_1(t)$ ($t = 0, T_1$). Taking into account the relation for the wave propagation velocity (1.3) and the fact that the water flow velocity of a long wave is constant in the entire water layer, the potential energy of a wave passing through the cross-section $x = x_1$ can be written down in the form

$$E_P = \int_0^{T_1} \frac{\rho g \eta_1^2(t)}{2} \times \sqrt{gD_1}\,dt \quad . \tag{1.11}$$

Let the wave in question reach a point x_2, the depth be equal to D_2, and the mareogram of the wave at the point x_2 be expressed by a function $\eta_2(t)$. However, the wave period has not changed and remains equal to T_1. It follows from the fact that, naturally, each wave segment passes the same way between the points x_1 and x_2 during the same time interval (no matter how the depth D_1 changes for D_2). Since the total energy of the wave remains constant and the potential energy of a moving wave always constitutes half the total energy (as is shown), the following integral equality is valid for the potential energy of the wave as it passes the cross-sections $x = x_1$ and $x = x_2$:

$$\int_0^{T_1} \frac{\rho g \eta_1^2(t)}{2} \times \sqrt{gD_1}\,dt = \int_0^{T_1} \frac{\rho g \eta_2^2(t)}{2} \times \sqrt{gD_2}\,dt \quad . \tag{1.12}$$

If the process of tsunami propagation is linear (as in the case of the deep ocean where the wave height is two orders lower than the depth), integral equality (1.12) is transformed to an approximate equality of the integrands (as is shown above). Therefore, after some simplifications we have

$$\eta_1^2(x) \times \sqrt{D_1} \approx \eta_2^2(x) \times \sqrt{D_2} \tag{1.13}$$

Hence, we have the approximate formula for the wave amplitude at the depth D_2:

$$\eta_2(x) \approx \eta_1(x) \sqrt[4]{\frac{D_1}{D_2}} \quad . \tag{1.14}$$

It is the well-known Green's formula describing a height variation of a long wave over an uneven bottom in the one-dimensional case. Thus, as a plane wave propagates from the deep ocean to a shallow-water shelf, its height increases proportional to the fourth root of the ratio between the initial and current depths (formula (1.14)). If a wave is not plane, its amplitude varies not only due to the non-constant depth, but also as a result of wave refraction (that is, the wave-front line transformation).

Let us consider a simple case of an initially circular tsunami wave propagating in an area of constant depth. In this case, according to Lagrange's formula (1.3), the wave front is always circular in shape with a constantly increasing radius, and the wavelength remains constant. It is clear that since the wave front extends, the amplitude steadily decreases. Let us use the energy conservation law to estimate the degree of this decreasing behavior. Let at some time instant the radius of the circular wave front be equal to R_1, at some other time, to R_2, and the lengths of the wave-front circles (arcs of the circle) be L_1 and L_2, respectively. Let us write down the wave potential energy taking into account the fact that the wave parameters are the same along the entire wave-front circle as follows:

$$E_P = \int_0^{L_1}\int_0^{\lambda_1} \frac{\rho g \eta_1^2}{2} d\lambda dl = \int_0^{\lambda_1} \frac{\rho g \eta_1^2}{2} L_1 d\lambda = \int_0^{L_2}\int_0^{\lambda_1} \frac{\rho g \eta_2^2}{2} d\lambda dl = \int_0^{\lambda_1} \frac{\rho g \eta_2^2}{2} L_2 d\lambda \quad . \tag{1.15}$$

Here λ_1 is the wavelength. In the case of a linear wave, integral equality (1.15) reduces to the equality of the integrands

$$\frac{\rho g \eta_1^2}{2} 2\pi R_1 = \frac{\rho g \eta_2^2}{2} 2\pi R_2 \qquad \eta_2 = \eta_1 \sqrt{\frac{R_1}{R_2}} \quad . \quad . \tag{1.16}$$

Thus, due to the cylindrical propagation the tsunami wave height decreases inversely proportional to the square root of the circular front radius or the wave front length.

In general, the kinematics of propagation of perturbations in various media is described by the eikonal equation (Romanov, 1984), which has the following form in the two-dimensional case:

$$\left(\frac{\partial f}{\partial x}\right)^2 + \left(\frac{\partial f}{\partial y}\right)^2 = \frac{1}{v^2(x,y)} \quad , \tag{1.17}$$

where v (x, y) specifies the velocity distribution in the medium. If the function f (x, y) is a solution to the eikonal equation (1.17), the wave front at the time T is described by the equation

$$f(xylem)=T, \tag{1.18}$$

and the equation $f(x, y) = 0$ specifies the perturbation source location or the initial wavefront line (the tsunami source boundary).

A concept of wave ray one of whose properties is the orthogonality to the wave-front line at any time is introduced in (Romanov, 1984). Along wave rays, a perturbation propagates from a source to other points of the medium in the least time. This means that wave rays are the fastest routes. Between the two closely spaced wave rays (in a ray tube), the wave energy remains constant (Romanov, 1984). Therefore, for a wave segment in a ray tube, formula (1.16) can be rewritten in the form

$$\eta_2 = \eta_1 \sqrt{\frac{L_1}{L_2}}, \tag{1.19}$$

where L_1 and L_2 are the widths of the ray tube (the length of the wave-front line segment inside the ray tube) at the initial and current time moments of wave propagation.

2. EXACT ANALYTICAL FORMULAS FOR WAVE-RAY TRACES ABOVE THE SLOPING BOTTOM

An exact mathematical formula for a wave ray trajectory over a sloping bottom can be found from the laws of geometrical optics. Consider a two-dimensional water area where the depth and the wave propagation velocity vary only in one direction. In this case we can use Snell's law for the wave ray refraction angle in a medium with varying optical conductivity (Sabra, 1981). According to this law, if in a two-dimensional conducting medium a ray comes at the angle of incidence α_1 to the horizontal line (Fig. 2.1), and the conductivity (propagation velocity of a signal) changes from b_1 to b_2, after passing the interface boundary its direction α_2 changes according to the formula

$$\frac{\sin(\alpha_1)}{b_1} = \frac{\sin(\alpha_2)}{b_2}. \tag{2.1}$$

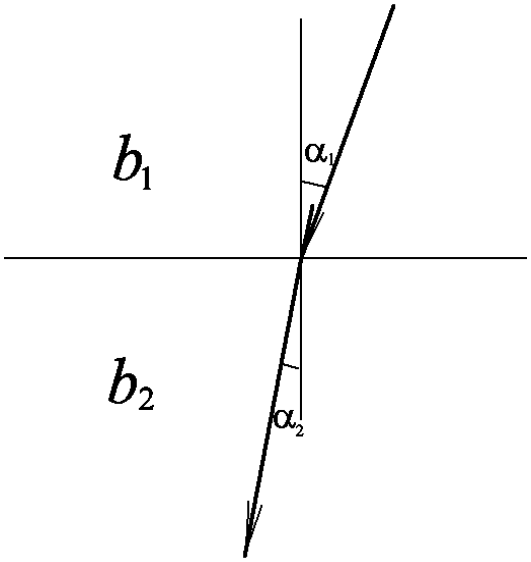

Figure 2.1. Wave ray refraction at the interface between two media

Thus, in a medium where the conductivity (wave propagation velocity) b varies only along one spatial variable (for instance, $b(y)$), the wave ray inclination from the direction of a change in the conductivity α changes according to the formula

$$\frac{\sin(\alpha(y))}{b(y)} = const1 = \frac{\sin(\alpha_0)}{b(y_0)} \quad . \tag{2.2}$$

Here α_0 is the initial incidence angle of the wave ray with respect to the vertical at the point $y=y_0$. In the case of a sloping bottom the medium conductivity (tsunami wave propagation velocity) is determined by Lagrange's formula (1.3), which for a sloping bottom has the following form:

$$b(y) = \sqrt{g \times y \times tg(\beta)} \quad , \tag{2.3}$$

where g is the acceleration of gravity, β is the bottom slope angle, and y is the distance to the coastline, where $y = 0$. Hence, the relation between the inclination angle (optimal trajectory) and the distance to the coast has the form

$$\sin^2(\alpha) = y \times \left(\frac{g \times tg(\beta) \times \sin^2(\alpha_0)}{b(y_0)^2} \right) = y \times \left(\frac{\sin^2(\alpha_0)}{y_0} \right) = const2 \times y \quad , \tag{2.4}$$

where the value of $const2$ is determined from the ray inclination at the distance y_0 to the coast ($0x$–axis). If α is assumed to be the parameter on which y depends, then from (2.4) we have

$$dy = \frac{2\sin(\alpha)\cos(\alpha)}{const2} \times d\alpha \quad . \tag{2.5}$$

Since ($\pi/2 - \alpha$) is the wave ray inclination angle (the graphic of the function $y(x)$) with respect to the horizontal direction, then according to the definition of the derivative of a function of one variable the following equality is valid:

$$\frac{dy}{dx} = \frac{\sin\left(\frac{\pi}{2} - \alpha\right)}{\cos\left(\frac{\pi}{2} - \alpha\right)} = \frac{\cos(\alpha)}{\sin(\alpha)} \quad ,$$

or

$$dx = dy\frac{\sin(\alpha)}{\cos(\alpha)} \quad . \tag{2.6}$$

From (2.5) and (2.6) we have

$$dx = \frac{2\sin(\alpha)\times\cos(\alpha)}{const2} \times \frac{\sin(\alpha)}{\cos(\alpha)} \times d\alpha = \frac{2\sin^2(\alpha)}{const2} d\alpha \quad . \tag{2.7}$$

Assuming that x and y depend on the parameter $u = 2\alpha$ and using trigonometric formulas for the sine and cosine of a double angle, we obtain the following formulas from (2.5) and (2.7):

$$dy = \frac{\sin(u)}{2\times const2} \times du \quad dx = \frac{1-\cos(u)}{2\times const2} \times du \quad , \tag{2.8}$$

Integrating equalities (2.8), we obtain the following equations for the wave ray trajectory in the parametric form:

$$x(u) = r(u - \sin(u)) + C_2$$

$$y(u) = r(C_3 - \cos(u)) \quad u \in [0, 2\pi] \quad , \tag{2.9}$$

$$r = 1/2 \times const2 = y_0 / 2\sin^2(\alpha_0) \quad .$$

This is a parametric form of the cycloid equation. Here the constants C_2 and C_3 are determined when the cycloid passes through the origin of coordinates. At the point (0,0) the parameter u is zero. This follows from Snell's law for the bottom in question (2.4). At $y = 0$, the angle α and the parameter $u = 2\alpha$ are zero. Hence, $C_2 = 0$, $C_3 = 1$. Finally, the wave ray equations in the parametric form are presented as

$$x(u) = r(u - \sin(u))$$
$$y(u) = r(1 - \cos(u)) \qquad u \in [0, 2\pi] \tag{2.10}$$

When the equations are written in this form, the parameter u is the doubled ray inclination angle with respect to the vertical direction and the coefficient r is determined in each specific case. In this boundary value problem for a wave ray, the parameter r is determined from the condition of ray passing through the point (x_1, y_1); here the second point is the origin of coordinates. For a wave ray which at offshore distance y_1 is directed at an angle α_1 with respect to the normal to the coastline ($0x$–axis), from (2.4) and (2.9) it follows that

$$r = \frac{y_1}{2 \times \sin(\alpha_1)} \tag{2.11}$$

Thus, we have obtained the equations describing the wave ray propagation above a sloping bottom using the laws of ray motion in a varying conductivity medium.

3. DETERMINATION OF A WAVE-FRONT LINE ABOVE THE BOTTOM SLOPE

For some model shapes of bottom, distributions of wave amplitudes (heights) can be found analytically. Consider, for example, a coastal area where the depth linearly increases with distance to the coast with a model source of tsunami in the form of a circle of radius R_0 with the center at the distance y_{00} from a straight coastline. In Fig. 3.1, this line coincides with the axis Ox ($y = 0$). In Section 2, the wave ray trajectory over a sloping bottom (as in the case in question) has already been found.

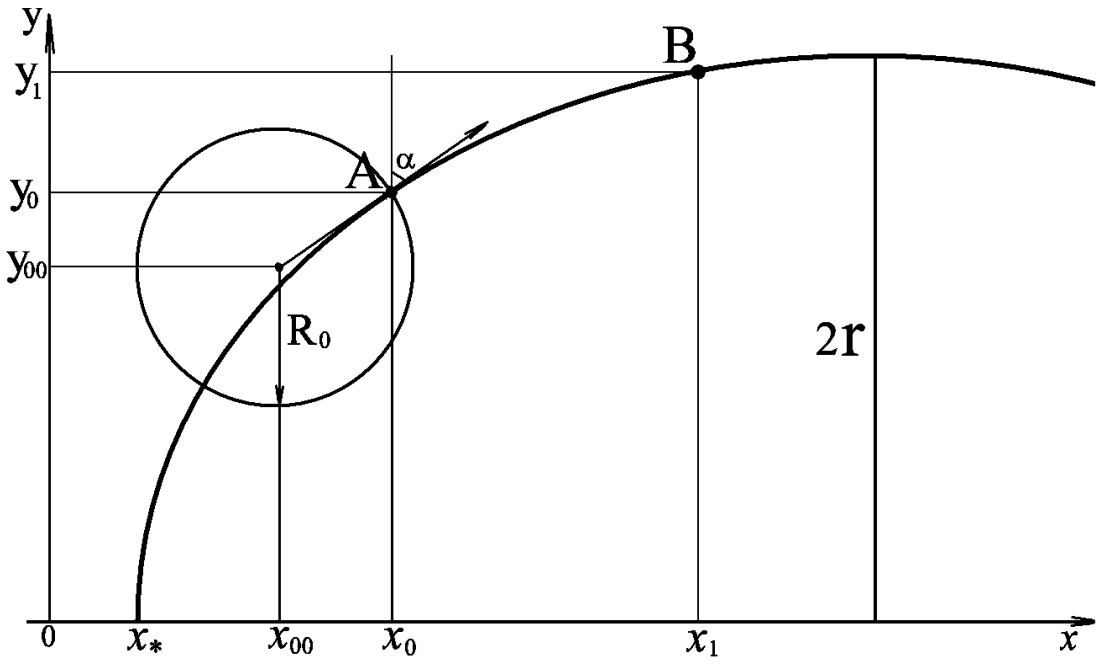

*Figure 3.1. A wave ray trajectory over a sloping bottom with inclination α with respect to the ordinate axis at the point **A***

If the depth is given by the formula

$$D(x, y) = a \times y \qquad (a > 0)$$
, (3.1)

then the wave ray trajectory (as has been found) has the form of a cycloid whose equations in the parametric form have the following form:

$$\begin{aligned} x &= r(u - \sin(u)) + x_* \\ y &= r(1 - \cos(u)) \end{aligned}$$
, (3.2)

Here x_* is the abscissa of reaching the coast by the cycloid, and r is its radius determined from its passage through given points or through its inclination angle at a certain distance from the coast. The parameter u is equal to the doubled inclination angle of a ray with the vertical. All parameters of the cycloid can be easily determined if the angle between the vertical and the tangent to the cycloid is known at some cycloid point. Thus, we construct a wave ray moving, at the angle α, from a point (x_0, y_0) located at the boundary of a circular tsunami source with radius R_0. Coordinates of the tsunami source center are (x_{00}, y_{00}) (see Fig. 3.1). The exit point coordinates are

$$\begin{aligned} x_0 &= x_{00} + R_0 \times \sin(\alpha) \\ y_0 &= y_{00} + R_0 \times \cos(\alpha) \end{aligned}$$
, (3.3)

The situation when the cycloid from the point **A**(x_0, y_0) goes up is somewhat different from the situation when it goes down. First consider the case when the angle α is in the interval (0, π/2) (see Fig. 3.1.) The radius of the cycloid can be easily calculated from formulas (3.2):

$$r = \frac{y_0}{1 - \cos(2\alpha)}$$
(3.4)

Let us obtain a formula for the time duration of the wave motion along this cycloid from the point (x_0, y_0) to the point (x_1, y_1). At the exit point **A**(x_0, y_0), the parameter u is

$$u_0 = 2\alpha$$
. (3.5)

This cycloid starts at the coastline point (x_*,0) (Fig. 3.1):

$$x_* = x_{00} + R_0 \times \sin(\alpha) - \frac{y_0}{1 - \cos(2\alpha)}\left(2\alpha - \sin(2\alpha)\right)$$
. (3.6)

Obtaining the radius from formula (3.4) and expressing the wave velocity in terms of the bottom topography (3.1) and Lagrange's formula (1.3), we can determine the time duration of wave motion along this cycloid from the point $\mathbf{A}(x_0, y_0)$ to the point $\mathbf{B}(x_1, y_1)$ in the form of the Fermat integral:

$$T = \int_A^B \frac{ds}{\sqrt{g \cdot a \cdot y}} = \int_A^B \frac{\sqrt{(r - r \cdot \cos(u))^2 + (-r \cdot \sin(u))^2}\, du}{\sqrt{g \cdot a \cdot r \cdot (1 - \cos(u))}} =$$

$$= \int_A^B \frac{r\sqrt{2(1 - \cos(u))}}{\sqrt{g \cdot a \cdot r \cdot (1 - \cos(u))}} du = (u_B - u_A)\sqrt{\frac{2r}{g \cdot a}} \quad , \qquad (3.7)$$

where $u_в$ and $u_а$ are values of the cycloid parameter at the points **B** and **A**, respectively. The value at the point **B** can be easily found from (3.2):

$$u_B = \arccos\left(1 - \frac{y_1}{r}\right) \quad . \qquad (3.8)$$

As was mentioned above, the parameter $u_а$ is equal to 2α. Finally, we obtain an expression for the time duration of wave motion from the point $\mathbf{A}(x_0, y_0)$ to the point $\mathbf{B}(x_1, y_1)$ as follows:

$$T = \sqrt{\frac{2r}{g \cdot a}} \cdot \left(\arccos\left(1 - \frac{y_1}{r}\right) - 2\alpha\right) \quad , \; 0 < \alpha < \pi/2 \; . \qquad (3.9)$$

Here the radius r is determined from (3.4). Now let us formulate the problem in a different way. Let the wave propagation time from the points of an initial circular front be known. We find the coordinates of the points along the corresponding wave rays, where the wave will arrive at the time T. For this, we first express $u_в$ from equation (3.7) in terms of the parameters of the cycloid and the time T. As a result, we have

$$u_B = u_A + T \cdot \sqrt{\frac{g \cdot a}{2r}} = 2\alpha + T \cdot \sqrt{\frac{g \cdot a}{2r}} = 2\alpha + \sqrt{\frac{g \cdot a \cdot (1 - \cos(\alpha))}{2y_0}} \quad , \qquad (3.10)$$

Now, from formulas (3.2) it is easy to find the coordinates of the wave front point in the wave ray in question at the time T:

$$x_1 = \frac{y_0}{1 - \cos(2\alpha)}\left(2\alpha + \sqrt{\frac{g \cdot a \cdot (1 - \cos(\alpha))}{2y_0}} - \sin\left(2\alpha + \sqrt{\frac{g \cdot a \cdot (1 - \cos(\alpha))}{2y_0}}\right)\right) + x_* \quad , \qquad (3.11)$$

$$y_1 = \frac{y_0}{1-\cos(2\alpha)}\left(1-\cos\left(2\alpha+\sqrt{\frac{g\times a\times(1-\cos(\alpha))}{2y_0}}\right)\right), \quad 0<\alpha<\pi/2. \tag{3.12}$$

If the exit angle α of the wave ray from the point (x_0, y_0) is in the interval $\pi/2 > \alpha > \pi$, formulas (3.11) and (3.12) can be slightly changed and written down as

$$x_1 = \frac{y_0}{1-\cos(2\alpha)}\left(2\alpha-\sqrt{\frac{g\times a\times(1-\cos(\alpha))}{2y_0}}-\sin\left(2\alpha-\sqrt{\frac{g\times a\times(1-\cos(\alpha))}{2y_0}}\right)\right)+x_*, \tag{3.13}$$

$$y_1 = \frac{y_0}{1-\cos(2\alpha)}\left(1-\cos\left(2\alpha-\sqrt{\frac{g\times a\times(1-\cos(\alpha))}{2y_0}}\right)\right). \tag{3.14}$$

When the exit angle α is equal to 0 or π the wave ray comes straight off or toward the coastline. Along these straight lines the wave travel time can be expressed as the route length divided by the arithmetic mean of wave velocities c_1 and c_2 at the start and destination points

$$T = \frac{y_1-y_0}{(c_1+c_0)/2} = \frac{2(y_1-y_0)}{\sqrt{g\times a\times y_1}+\sqrt{g\times a\times y_0}}, \quad y_1 > y_0. \tag{3.15}$$

In order to obtain the ordinate y_1 of the wave isochrone along these two rays it is necessary to solve the following equation

$$f\times\left(\sqrt{y_1}+\sqrt{y_0}\right) = y_1-y_0 = \left(\sqrt{y_1}+\sqrt{y_0}\right)\left(\sqrt{y_1}-\sqrt{y_0}\right), \quad f=\frac{T\sqrt{ga}}{2} \tag{3.16}$$

Finally, the formulas for the solutions y_1 are as follows:

$$y_1 = \left(\sqrt{y_0}+f\right)^2, \quad y_1 > y_0 \text{ and } y_1 = \left(\sqrt{y_0}-f\right)^2, \quad y_1 < y_0. \tag{3.17}$$

Thus, we have obtained the coordinates of the destination point versus time T and the angle α. Now, with formulas (3.9) and (3.10) we can find the wave front location by fixing the time T and taking the values α in the entire interval $(-\pi, +\pi)$ with a sufficiently small step $\Delta\alpha$. It should be noted that in the case of a circular initial tsunami front the value of x_* and the coordinates of the wave ray exit points (x_0, y_0) vary according to formulas (3.6) and (3.3). Figure 3.2 presents the wave rays from the circled source boundary using formulas (3.11)-(3.14) and (3.17).

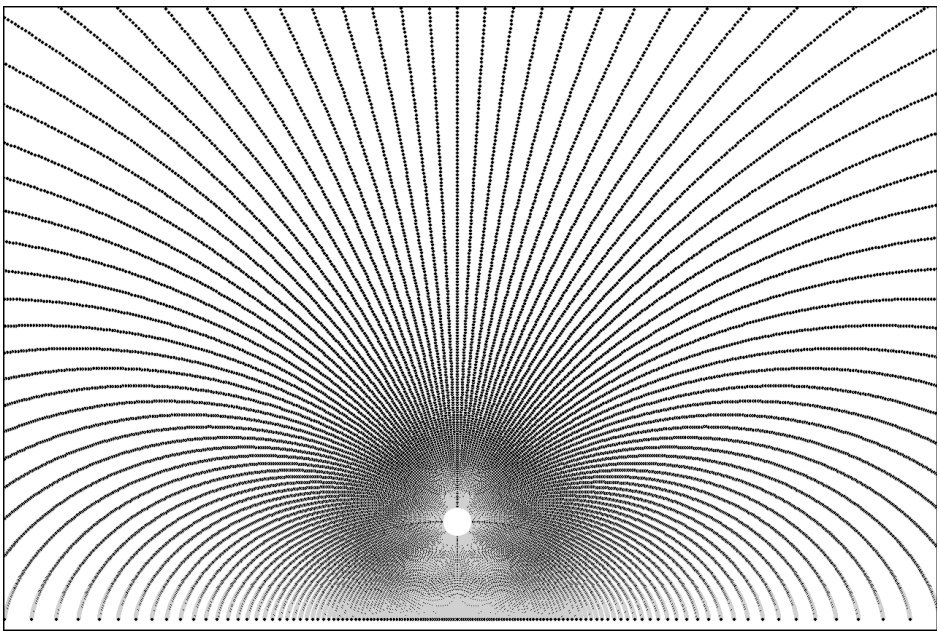

Figure 3.2. Traces of wave rays from the round source boundary above the bottom slope

If we draw the lines connecting points along wave the rays corresponding to the same time instance, then we will obtain tsunami isochrones. For example, Figure 3.3 shows locations of the wave front within 5 minutes interval.

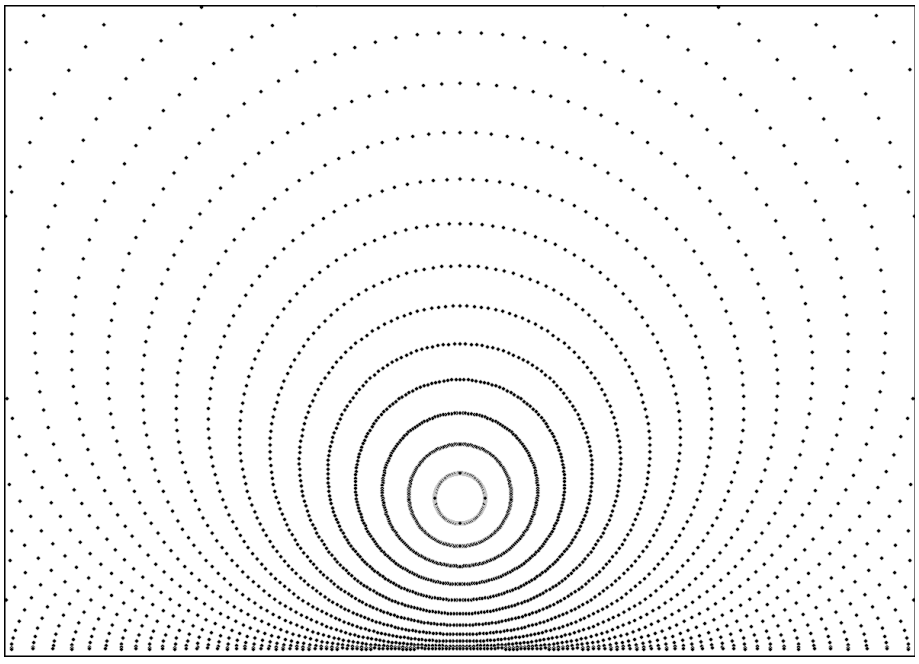

Figure 3.3. The shapes of tsunami isochrones from the round-shaped source within 5 minutes interval

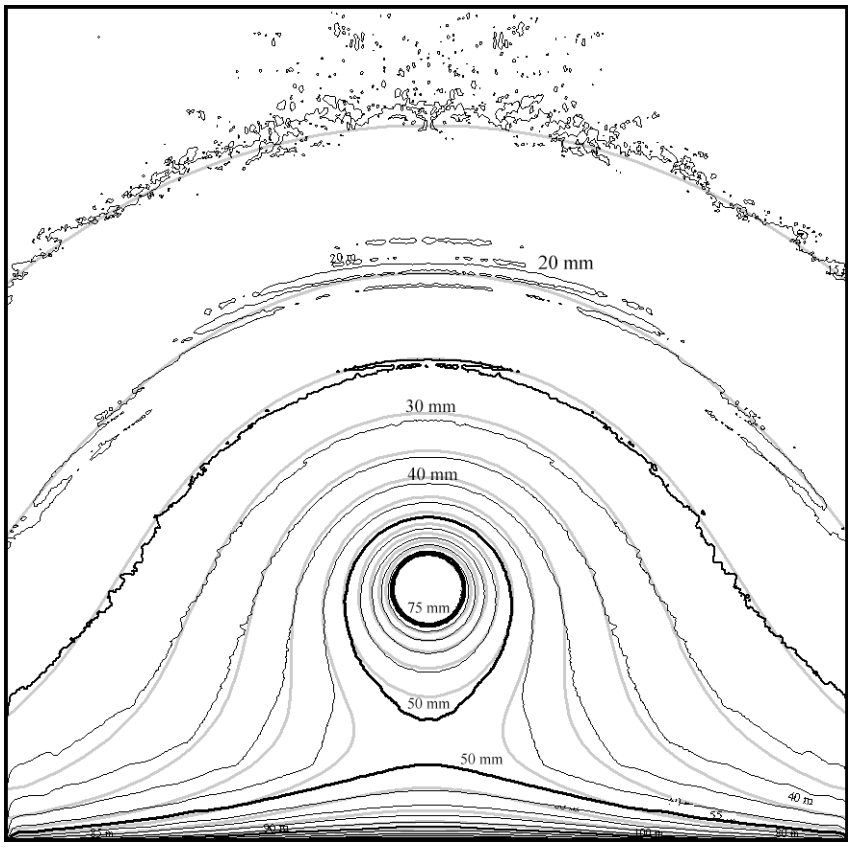

Figure 4.1. Comparative location of isolines of tsunami height maxima calculated by the numerical shallow water model (Titov, Gonzalez, 1997) (black color) and by the ray approximation (grey color)

4. ESTIMATION OF THE TSUNAMI WAVE HEIGHT WITHIN THE WAVE-RAY APPROXIMATION

If we want to estimate the wave height at the point (x_1, y_1) it is necessary to determine the distance between two points. The first one is the point (x_1, y_1), where the wave going along the ray exiting the point $(x_{00}+R0 \sin \alpha, y_{00}+R_0 \cos \alpha)$ at the angle α (fig. 3.1) arrives at the time T. The second one is the point (x_2, y_2), where a tsunami wave arrives at the same time moment going along the wave ray exiting the point $(x_{00}+R_0 \sin(\alpha+\Delta\alpha), y_{00}+R_0 \cos(\alpha+\Delta\alpha))$ at angle $\alpha + \Delta\alpha$. With formulas (1.19) and (1.14), the coefficient of wave attenuation due to changing the ray tube width and depth is calculated. Doing this for various values of the time T and the directions of wave rays, we obtain the wave attenuation distribution over the entire area of points which can be reached by the wave rays from the initial wave front points. To verify the solution obtained, the numerical simulation of tsunami wave propagation was carried out using the differential shallow-water model with a package called MOST (Titov, Gonzalez, 1997). In this numerical experiment, the center of a circular 2 m height source, 40 km in radius, was located at a distance of 300 km from the coast. This source formed a 75-cm high circular wave at a distance of 43.6 km from the center. This initial front was taken as initial conditions to

calculate the amplitudes with the ray model. In Fig. 3.4, isolines of the tsunami wave height maxima in a 1000 × 1000 km coastal area with a sloping bottom obtained from formulas (3.11)–(3.14) and (3.2) are shown by grey color. For comparison, isolines of the wave height maxima obtained by numerical solution of the same problem with the shallow water model having the same initial values are shown by black color. In both cases, the levels of isolines (whose height is shown in cm), were taken with a spacing of 5 cm. The figure 3.4 shows that the distributions of amplitudes obtained by the two different methods mostly coincide. An exception is a coastal band where, in contrast to the ray approximation, the numerical implementation of the differential shallow water model uses the boundary conditions of the full reflection at the coastline. This approximately doubles the height of the wave that arrives there.

CONCLUSIONS

The height of a propagating tsunami wave versus depth and refraction above an uneven bottom has been estimated from the differential shallow-water equations. The exact wave ray trajectory and tsunami isochrones above a sloping bottom has been found. A comparison of the results obtained by the ray method and with the shallow water model has been made. It shows that with a numerical method based on the ray approximation not only the arrival times of tsunami waves at different points, but also the wave heights can be estimated. These benchmark solutions can be used for testing the numerical methods in the tsunami modeling.

REFERENCES

1. Stocker J.J., Water Waves. The Mathematical Theory with Applications.— New York: Interscience Publishers, 1957.
2. Marchuk, An.G., Chubarov, L.B., and Shokin, Yu.I., Chislennoe modelirovanie voln tsunami (Numerical Simulation of Tsunami Waves), Novosibirsk: Nauka, 1983.
3. Romanov V.G., Inverse Problems of Mathematical Physics, VSP, Netherlands, 1984.
4. Sabra A. I., Theories of Light from Descartes to Newton, Cambridge University Press, 1981 (cf. Pavlos Mihas, Use of History in Developing ideas of refraction, lenses and rainbow, p. 5, Demokritus University, Thrace, Greece.)
5. Titov V.V., Gonzalez F., Implementation and testing of the method of splitting tsunami (MOST) // Technical Memorandum ERL PMEL-112, National Oceanic and Atmospheric Administration. — Washington DC, 1997.

ISSN 8755-6839

SCIENCE OF **TSUNAMI HAZARDS**

Journal of Tsunami Society International

Volume 35 **Number 2** **2016**

THE TROBRIAND ISLANDS EARTHQUAKE AND TSUNAMI, 6 MARCH 1895

Horst Letz[1], Kevin McCue[2] and Ian Ripper[3]

[1] GeoForschungZentrum Potsdam, Germany, [2]Australian Seismological Centre, Canberra, Australia, [3]Brisbane Queensland Australia.

ABSTRACT

An earthquake and tsunami struck the Trobriand Islands in March 1895 causing at least 30 deaths but until now the location and magnitude of the earthquake were quite uncertain. We have searched British and German colonial literature of the time to refine both parameters of Everingham's original estimates. Our magnitude of 7.3±0.3 and location at (8.4°S, 150.1°E) compare well with Everingham's magnitude 7-8 and (9°S, 151°E). Whilst the earthquake seems to be associated with the Trobriand Trench, very few others have occurred there since modern seismographs were deployed in the mid-1960s, certainly none of magnitude 7 or more, none with a thrust mechanism and none that have generated a destructive tsunami. We compare this earthquake and tsunami with the 1998 Sissano Lagoon earthquake, for which we have drawn an isoseismal map, and briefly discuss the implications for tectonic interpretation and hazard assessment.

Vol. 35, No. 2, Page 49, (2016)

INTRODUCTION

The island of New Guinea is at the corner of a collision zone between the Pacific and Indo-Australian Plates with several plate fragments or small plates wedged between them. Many researchers have studied or commented on the seismicity of this most interesting area including Richter (1954), Brooks (1965), Denham (1969, 1973, 1974), Everingham (1973, 1974, 1975, 1977), Ripper and Letz (1991, 1993), McCue (1984), Tregoning and others (1998) and most recently Anton (2009) but there is no consensus on a tectonic model.

It is always rewarding to investigate 'rogue' earthquakes that don't appear to fit the models and this was the impetus to investigate this large tsunamigenic earthquake in the Solomon Sea in 1895. At that time Germany controlled the northern half of eastern New Guinea, New Britain, New Ireland and Bougainville, while Great Britain claimed sovereignty over the southern half of eastern New Guinea (known today as the Independent State of Papua New Guinea), while the Dutch ruled over west New Guinea (now the Papua Province of Indonesia).

THE 1895 EARTHQUAKE

One of the first reports of the earthquake and possible aftershocks to reach the outside world was published in New Zealand in the *Grey River Argus*, Volume XXXVII, Issue 9093, 25 March 1895, Page 4, just two weeks after the earthquake. The shaking from not one but a series of earthquakes was felt in Port Moresby but clearly not on Thursday Island.

The following extract from *The Queenslander* of Saturday 25 May 1895, Page 1000 is typical of the descriptions in the contemporary Australian media and German reports.

> *The Acting Administrator of British New Guinea, in a despatch dated the 1st April, gives the following account of an earthquake and tidal wave experienced in the Possession on the 6th March last, obtained from an intelligent native of the island of Sim-Sim :— A little after sunset they experienced a shock, then followed a loud booming sound apparently not very far off, then another shock. After this there was a lull, and then they heard the noise of the advancing wave, which almost immediately afterwards swept over the flat. The waters knocked the frail native houses down and swept portions of them, together with household goods, into the sea. One child was drowned, and one man received severe abrasions of the skin. Those of the natives who did not manage to grasp the trunks of trees were washed into the sea. Our informant said that he caught hold of a cocoanut tree, and that the water reached to his armpits.*

Other reports indicate that the sea receded a considerable distance after the earthquake before crashing back onto the island. *The Queenslander* of 4 May 1895 reports:

> *It appears that on the night of the 6th March the islands received the full force of an earthquake, with a tidal wave, which swept everything before it. The natives are awfully frightened, and they informed us that the salt water left them at 6 p.m. on the 6th, and they could see the bottom of the sea quite dry for miles around them, when all of a sudden they*

could see a great cloud of water making towards them with an awful roar, which frightened them so that they all made for the cocoanut trees, where they remained until the great cloud of water passed over the islands.

In Nachrichten über Kaiser Wilhelms-Land und den Bismarck-Archipel, Ausgabe 1895, Page 52, missionary J. G. Pfalzer reports a very strong earthquake from his location in Simbang (near Finschhafen):

*On 6 March 1895, around 7 o'clock in the evening, a very strong earthquake was felt, not excessively violent or jerking pushes, but a strong, regular shaking like being in a strainer, that, perhaps, lasted for a few minutes. Immediately, I heard a strong quenching of the sea that quickly increased in intensity. I ran to the beach and the sea surface was strongly disturbed. It was an abnormal tidal wave that looked the same as on 13 March 1988 [*Authors: Tsunami associated with the Ritter Island eruption and collapse*]. Every 5 minutes a change from falling tide to rising tides, with the surge of 2 feet above the highest tide mark and the falling tide about 1 foot below the lowest mark of low tides. Although, the tide returned with great might, carrying-over and destroying everything that was within reach, boats, trees, etc.. This scenario lasted until 10 o'clock (in the evening), then the waves eased off and later on the moonlight gleamed on a glassy ocean surface.*

A location and magnitude of the earthquake were first tabulated by Everingham (1977) who estimated the magnitude as between 7 and 8 and the (uncertain) location at (9°S, 150°E). He reprinted reports and observations of the earthquake and tsunami, all sourced from the British administered Papua region. A search of the ISC database resulted in no events but NOAA reports the earthquake and tsunami as follows with a slightly different location, a magnitude of 7.5, a puzzling focal depth of 170km, and source unspecified:

Date	Time UTC	Mag	Location	Latitude	Longitude	Depth
18950306	08 35	7.5	W. Solomon Sea	-8.5	151.0	170

Other anecdotal accounts of the earthquake and tsunami were found in newspapers in the Australian National Library using their on-line search facility TROVE. It is interesting to note that the first reports of this earthquake received in Australia were from the crew of a German steamer *Isabel* that arrived in Sydney in mid-April 1895. It was also felt and later reported as a strong jolt by the crew of *Merrie England* anchored near the island of Jaga (Yaga) in the Trobriands.

Contemporary German sources from the northern side of New Guinea and Neu-Pommern (today's New Britain), archived in Berlin, were investigated for this study. The felt reports from both sources are mapped and the approximate felt area drawn as shown in Figure 1 to constrain both the location

(the approximate centre of the felt area) and magnitude (the size of the felt area by comparison with the felt area during later earthquakes with measured magnitudes in the region, mostly data from Port Moresby Geophysical Observatory reports).

There are few earthquakes located on the Trobriand Trench and this is the largest of them by far, and the only one known to have caused a destructive tsunami. Duda (1965) is alone in ascribing a location near the Trobriand Trough to a M 7.8 earthquake on 24 January 1902 at 23:27 UTC but this is not confirmed by other sources who attribute it to the plate boundary further north. The shaking in 1895 was not felt in Herbertshöhe (Kokopo near Rabaul) but was felt in Madang for example, and the tsunami was very localised, damaging just the Trobriand Islands and the east Papua Peninsula coast where three villages were destroyed, their occupants killed (annual report for British New Guinea tabled in the Australian Parliament). The very localized destruction was mirrored in the 1998 Sissano Lagoon earthquake and tsunami. Reports indicate the maximum run-up was about 6m. By analogy with the 1998 earthquake on the north coast, we infer that the source was a shallow, tsunamigenic earthquake and not just a simple shallow thrust. Neither a normal nor a strike-slip source would generate such a large, localised tsunami following an earthquake of this moderate magnitude.

The location must have been very local to the Trobriands as evidenced by the following observation at Sim-Sim (*The Queenslander* of 25 May 1895):

> *A little after sunset they experienced a shock, then followed a loud booming sound apparently not very far off, then another shock. After this there was a lull for a short time, and then they heard the noise of the advancing wave, which almost immediately afterwards swept over the flat*.

We surmise that this was the basis for Everingham's experienced assessment of the location. Another clue as to the location is that the wave struck the island of Sim-Sim on its western side so the focus was surely west of Sim-Sim, most probably within 50km of this location and perhaps less than 25km at (8.4°S, 150.1°E).

The listed place names and coordinates as shown in Figure 1 are in Table 1.

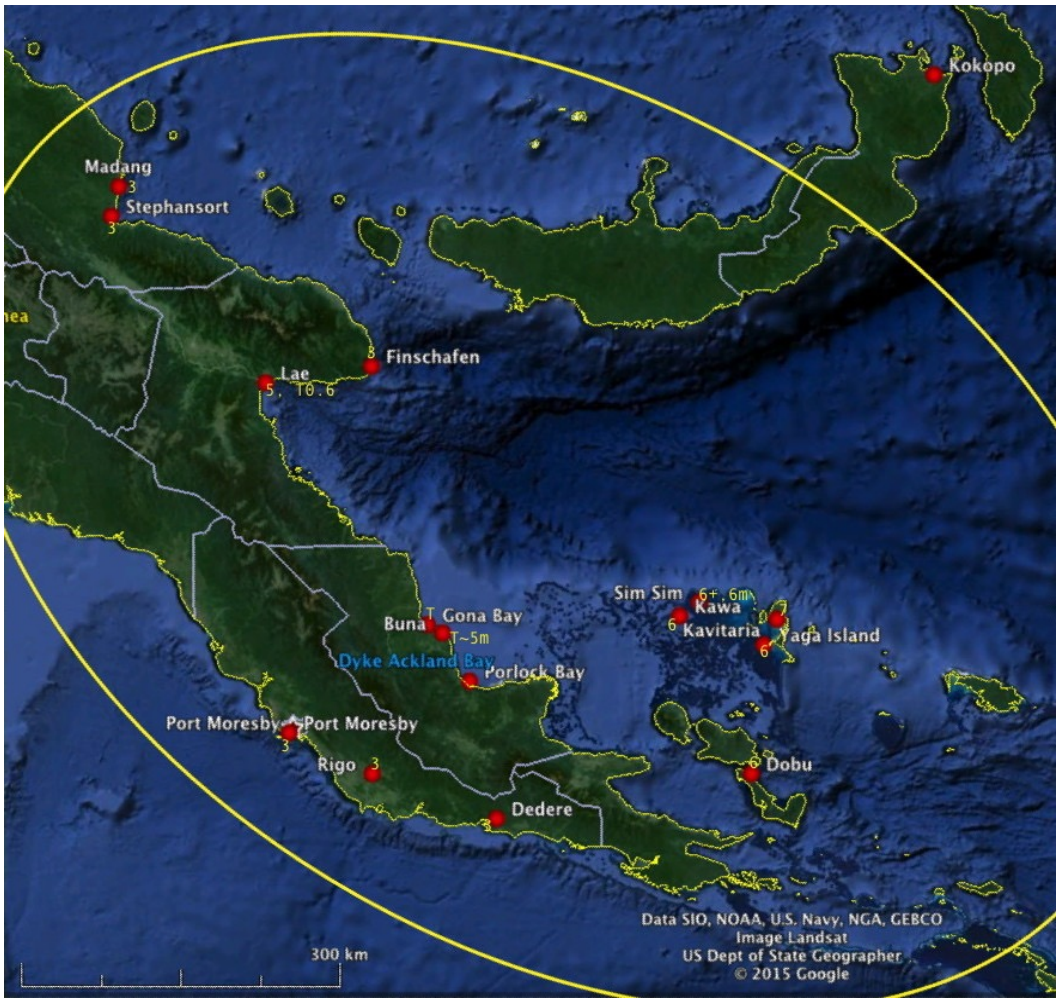

Figure 1. Felt area of the 6 March 1895 earthquake in the Trobriand Islands. The MM Intensity is given followed by the tsunami runup height (6, 6m) or just the tsunami height T~5m where reported or estimated.

Table 1. Places where the 1895 earthquake shaking was reported felt

Place	Lat °S	Long °E	MMI	Comment
Port Moresby	9.4	147.2	3	Felt
Dedere (Abau)	10.2	148.7	3	Felt
Rigo	9.8	147.8	3	Felt
Kokopo	4.3	152.3	0	Not felt

Yaga Trobriand Is	8.74	150.96	6+	Felt onboard, ship heaved and trembled for a minute.
Kavatari	8.54	151.04	7	Trees swayed, liquefaction observed
Sim-Sim Island or Kumkwalego	8.42	150.45	6+	Strong shaking and 6m tsunami. One report mentions that the water receded first.
Dobu	9.75	150.87	6+	
Madang	5.2	145.8	3	
Finschhafen	6.6	147.8	3	
Stephansort	5.45	145.7	3	
Simbang near Finschafen	6.58	147.83	5	Strong but not jerky, small tsunami
Kawa	8.52	150.32	6	Shaking dislodged large coral overhangs but no tsunami

Various estimates of the earthquake source details are summarised in Table 2.

Various estimates of the earthquake source details are summarised in Table 2.

Table 2. Parameters of the 1895 earthquake

Date	Time UTC	Lat °S	Long °E	Mag	Ref	Comments
1895 03 06	08:35	9	150	7-8	Everingham	
		8.5	151.0	Ms 7.5	NOAA	50-100 dead no reference.
		8.4	150.1	Ms 7.3	This report	More than 30 deaths

Whilst preparing this paper we looked at the felt reports for the 1998 Sissano Lagoon earthquake listed by Ripper and others (1999) to add to the intensity attenuation database. Some reports were recently found of the impact in Papua Province Indonesia (Joku, 1999) where it was felt as far as the capital Jayapura. From these reports we were able to draw an isoseismal map.The felt area is very similar to that of the magnitude 7 October 1968 Wewak earthquake (Denham, 1974). The offset of the high intensity shaking from the computed epicentre and area of maximum tsunami run-up is obvious in the inset Figure 2. The three epicentres are widely scattered indicative of the high uncertainty in the focal region, at least a source length apart, and this today let alone 100 years ago.

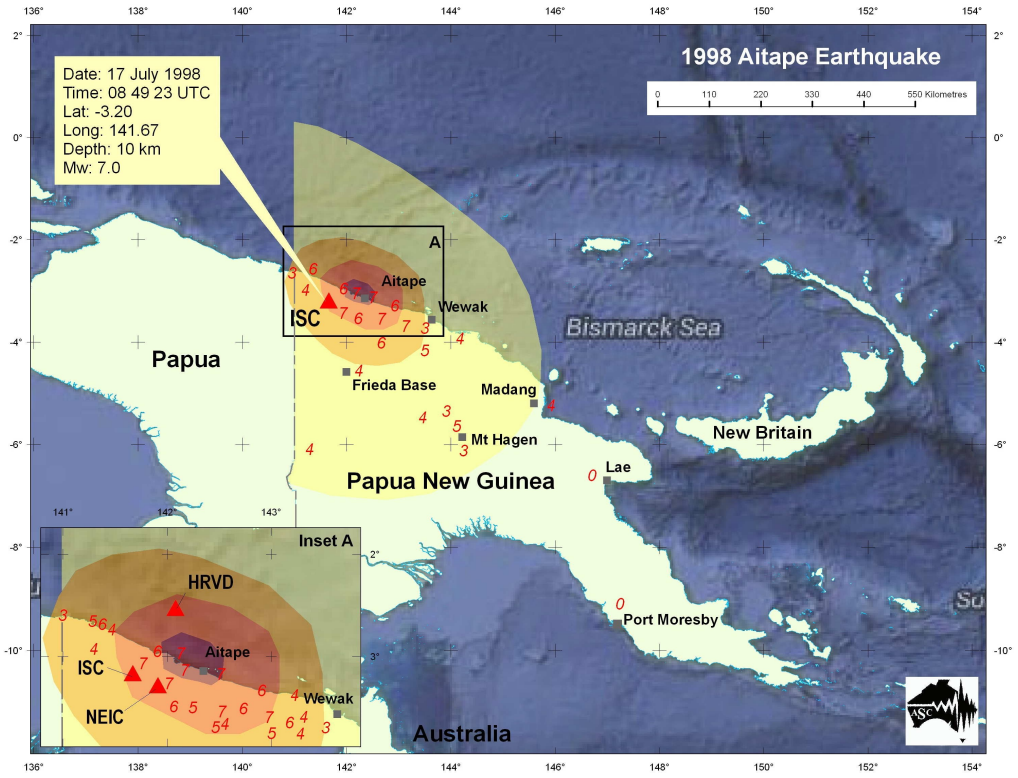

Figure 2. Isoseismal Map, MM intensity, of the destructive July 1998 Sissano Lagoon tsunamigenic earthquake.

THE MAGNITUDE ESTIMATE

The felt area is elongated along the axis of the Trobriand Trench as shown in Figure 2. The half-long axis or radius of perceptibility (Rp) along the major axis is about 575 km from the supposed epicentre NW of Sim-Sim Island to Madang. By comparison we have plotted the radius of perceptibility against magnitude (M) for other major earthquakes in Papua New Guinea, most of them around the Solomon Sea (Table 3, Figure 3), and obtain the following approximate equation:

$$M = 1.8 \ln Rp - 4.1$$

and from this we obtain a magnitude of 7.3. Perhaps the best comparison is with the October 1968 Wewak and 1970 Madang earthquakes, neither of which were felt as far as the Trobriand Islands. The ground shaking in the 1970 Madang earthquake was along the same path in reverse as the 1895 earthquake which would suggest a magnitude nearer 7 than 8. Our best estimate of magnitude is 7.3±0.3.

Table 3 Magnitude and radius of perceptibility from published isoseismal maps.

Date		Felt radius along long axis	Author	Location
20 Jul 1975	7.5	600	Everingham	Bougainville
9 Mar 1979	6.2	390	McCue	Papuan Peninsula
26 Jul 1971	8	720	Everingham	N Solomon Sea
14 Jul 1971	8	585	Everingham	N Solomon Sea
31 Oct 1970	7	625	Everingham	Madang
11 Apr 1978	5.7	175	McCue	Papuan Peninsula
23 Oct 1968	7	404	Denham	Wewak
5 Sep 1968	5.6	285	Denham	Southern Highlands
16 Sep 1976	5.9	370	McCue	Papuan Peninsula
17 Jul 1998	7.0	410	This paper	Sissano Lagoon

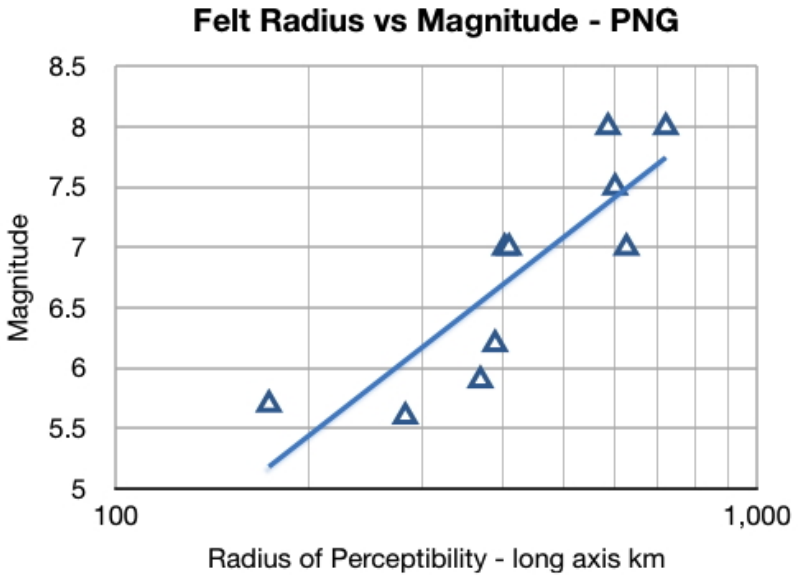

Figure 3. The felt radius, along the long or major axis of isoseismal maps of selected earthquakes in Papua New Guinea, versus magnitude. Events are listed in Table 1.

TSUNAMI

Reports indicate that the tsunami was very localised and/or directional, the water receded first then returned as a 6m high tsunami at Sim-Sim yet no impact was observed on Kawa only 20km away. A 'great wave' was reported in Porlock Bay on the Papuan Peninsula west of the Trobriand Islands where four villages were washed away, some of the villagers drowned. At Buna it is reported that 26 people drowned (Everingham, 1977). We have assumed the tsunami height there was 3 to 5m to cause the damage reported. At Simbang (near Finschhafen) the detailed sea-level observations made by missionary J. G. Pfalzer (Appendix 3) describe a typical tsunami with run-up of about 1m:

> *every 5 minutes a change from falling tide to rising tides, with the surge of 2 feet above the highest tide mark and the falling tide about 1 foot below the lowest mark of low tides. Although, the tide returned with great might, carrying-over and destroying everything that was within reach, boats, trees, etc. This scenario lasted until 10 o'clock (in the evening), then the waves eased off.*

Pfalzer measured both the period, 5 minutes is very short, and amplitude above and below the tidal limits. The maximum tidal range in the Huon Gulf at Lae is 1m so the actual tsunami run-up would have been about 1m at Simbang.

The tsunami is listed by the Russian Tsunami Laboratory Institute of Computational Mathematics and Mathematical Geophysics SB RAS Tsunami Laboratory, Novosibirsk, Russia in their Web Encyclopedia on Natural Hazards.

TECTONICS

There are as many models of the plate geometry in the Papua New Guinea region as there are publications on the subject as noted by Tregoning and others (1998), but they are not well constrained by the seismicity as shown in Figure 4. In particular the lack of seismicity along the Trobriand Trench is noticeable.

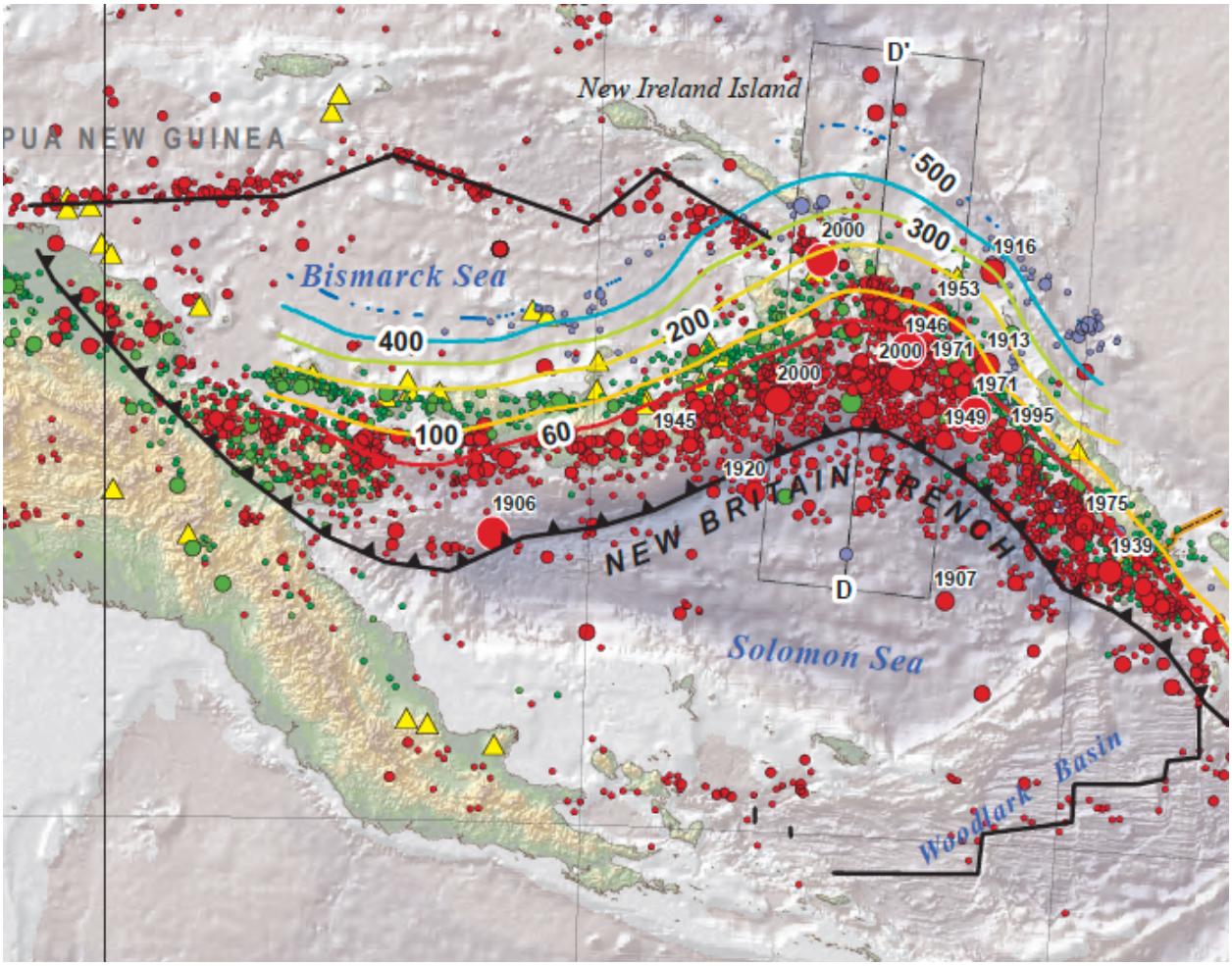

Figure 4. Seismicity of the Solomon Sea region (from Benz and others, 2011). The red dots are for earthquakes less than 70km deep, green dots for depth 70 – 299km and blue dots depth of 300km or more. The yellow triangles show some of the active volcanoes. There is remarkably little seismic activity to suggest that the Trobriand Trough is active. Researchers have based their models heavily on the topography or bathymetry rather than the seismicity.

A search of the ISC database from 1900 to 2012 centered at (8.5°S, 150°E) and radius of 1.5° yielded just 2 large (M > 5.9) earthquakes both of them between the New Britain Trench and the Trobriand Islands (Figure 5). Details of these two events are listed below.

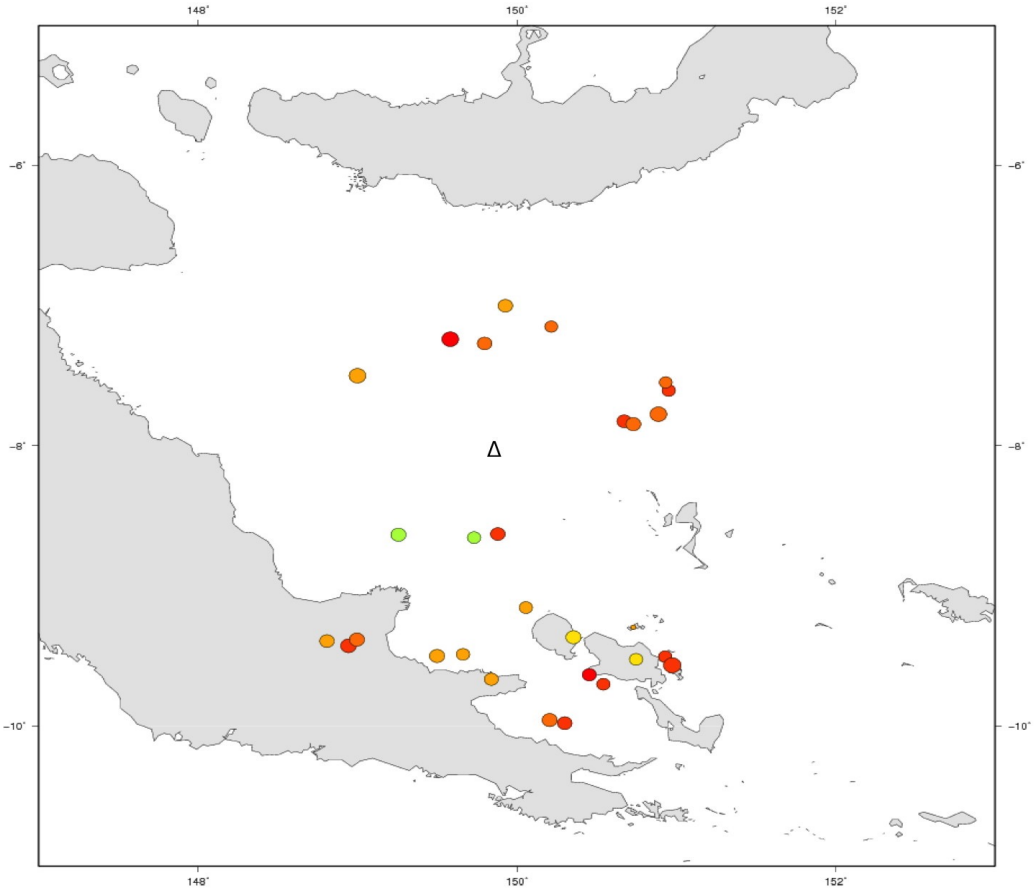

Figure 5. Seismicity from the ISC for the period 1900 – 2012, M≥5.5, centred on the triangle near (8°S, 150°E) and radius 1.5° (to mask the New Britain Trench seismicity). The Trobriand Trench is not defined by the seismicity, just a few scattered epicentres north and northwest of the Trobriand Island.

1. 1975/02/07 04:51:40 7.24°S 149.58°E 9 Ms 6.4 (NEIS) ISC

This large Ms 6.4 shallow earthquake to the northwest of the Trobriand Islands was below the Trobriand Trench, felt widely notably at Rabaul (note that the 1895 event was reported not felt at nearby Kokopo). No mechanism was computed.
(Felt I=IV MM Kandrian, Gloucester, III Popondetta, Salamoa, Rabaul, II-III Esa'ala, Bolubolu, I-II Tufi, Sanaroa. Also Felt at Losua.)

This is a well-constrained location, surrounded by seismographs of the then extensive PNG network, the gap only 22°. The depth too is well controlled, 9 ± 7km, supported by depth phases such as PcP.

2. 2000/07/16 03:57:48 7.78°S 150.89°E 12 Mw 6.6 (HRVD) ISC
This large shallow (12km deep) earthquake north of the Trobriand Islands below the Trobriand Trench is from the ISC.

None of the nodal planes parallels the strike of the Trobriand Trough. They are more likely fractures in the outer rise of the Solomon Sea plate subducting under New Britain.

Three computed focal mechanisms for this earthquake are shown in Figure 6. They can't all be right, maybe none are right, but none of them are shallow thrusts as would be expected if the Trobriand Trough subduction zone was the source.

Figure 6. Focal mechanisms published by the ISC for the 16 July 2000 earthquake in the west Solomon Sea. Note that the HRVD mechanism (3rd image) and one of the two NEIS mechanisms (2nd image) are 'normal', the other a strike-slip mechanism, not thrusts as supposed by models of a subducting slab at the Trobriand Trench.

http://volcano.oregonstate.edu/vwdocs/volc_images/southeast_asia/papua_new_guinea/tectonics.htm (accessed on 30 May 2015).

Bird (2003) shows a more extensive Woodlark Plate (Figure 7.1) than other authors such as Hamilton, 1979 in Figure 7.2. The proposed tectonic configuration by Taylor and others (1991) and Tregoning and others, 1998 are shown for comparison with our postulated model influenced strongly by the seismicity.

http://swpacificplates.weebly.com/caroline-north-bismarck-south-bismarck-manus.html (accessed on 30 May 2015).

http://volcano.oregonstate.edu/vwdocs/volc_images/southeast_asia/papua_new_guinea/tectonics.htm (accessed on 30 May 2015).

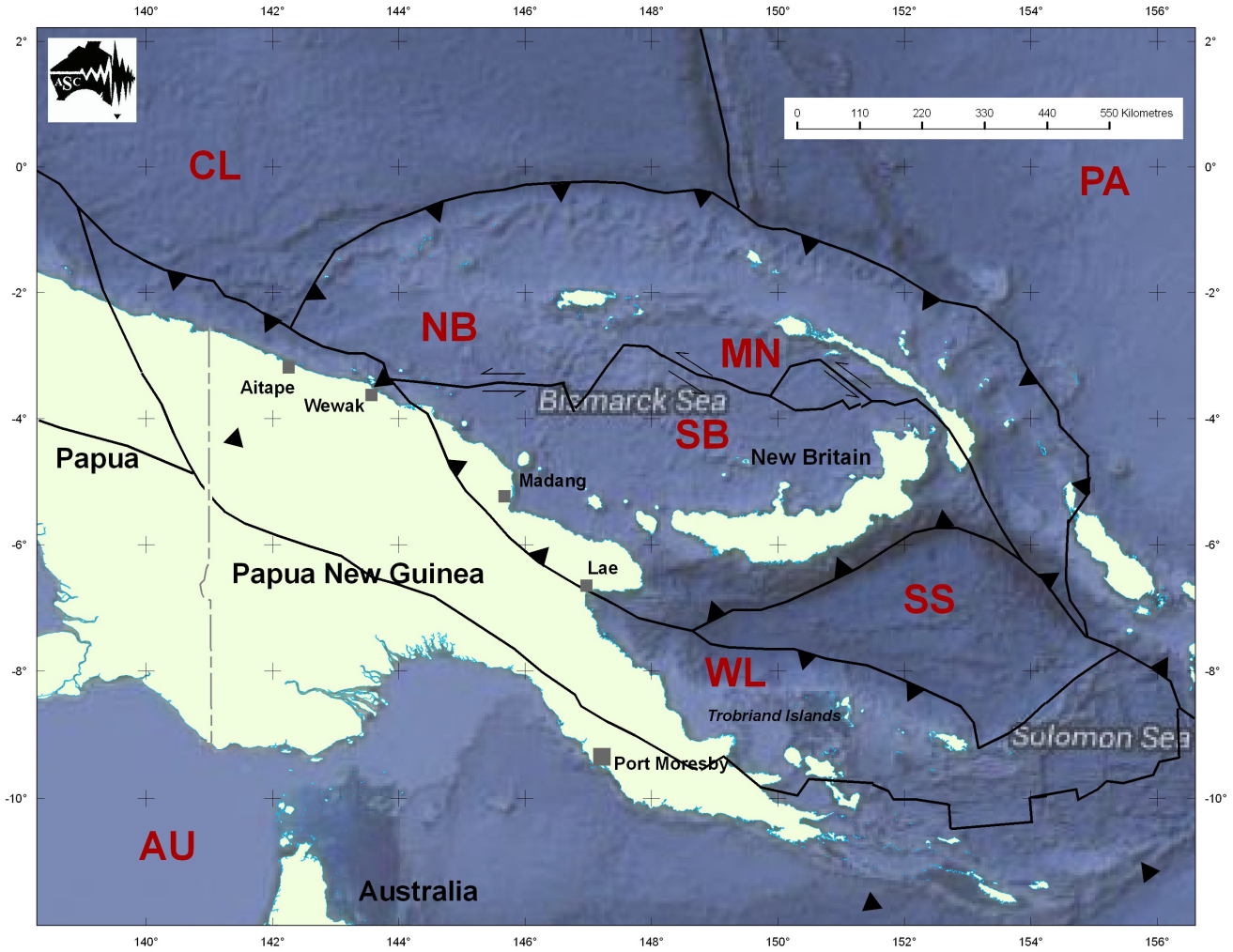

Figure 7.1 Plate configuration by Bird (2003) and Kelsey Lamothe. AU, CL, MN, PA, NB, SB, SS, WL are their postulated Australian, Caroline, Manus, Pacific, North Bismarck, South Bismarck, Solomon Sea and Woodlark Plates. Their Woodlark Plate extends from the Solomon Trench through the New Guinea Highlands to the Caroline Plate.

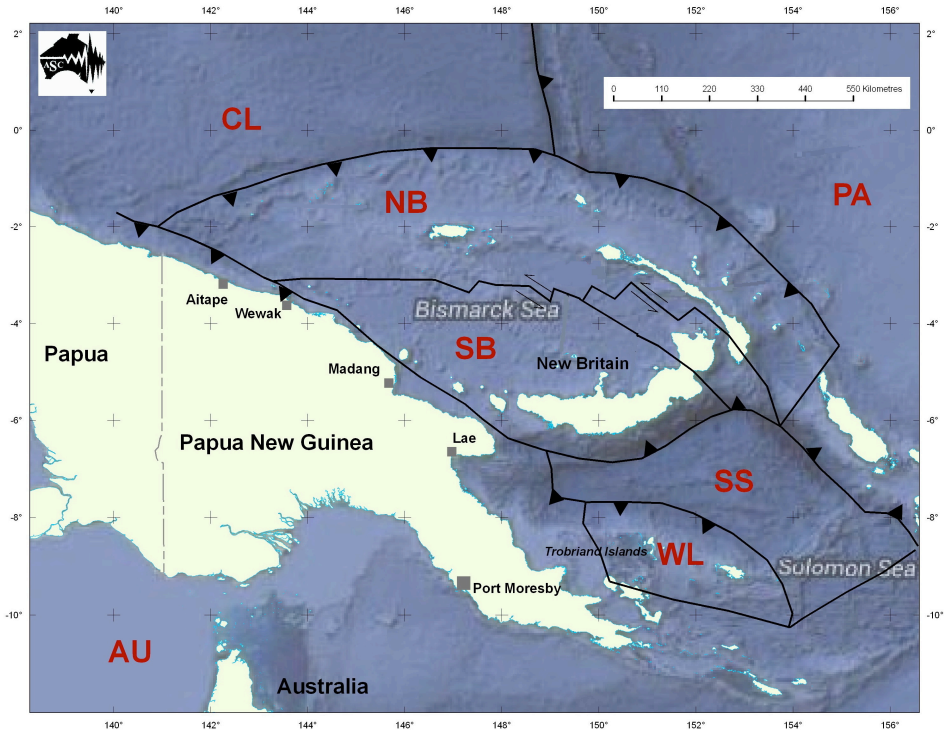

Figure 7.2 Plate configuration by Oregon State University (simplified from Hamilton 1979). They show an active Trobriand Trench where a Solomon Sea Plate (SS dips under a Woodlark Plate (WL).

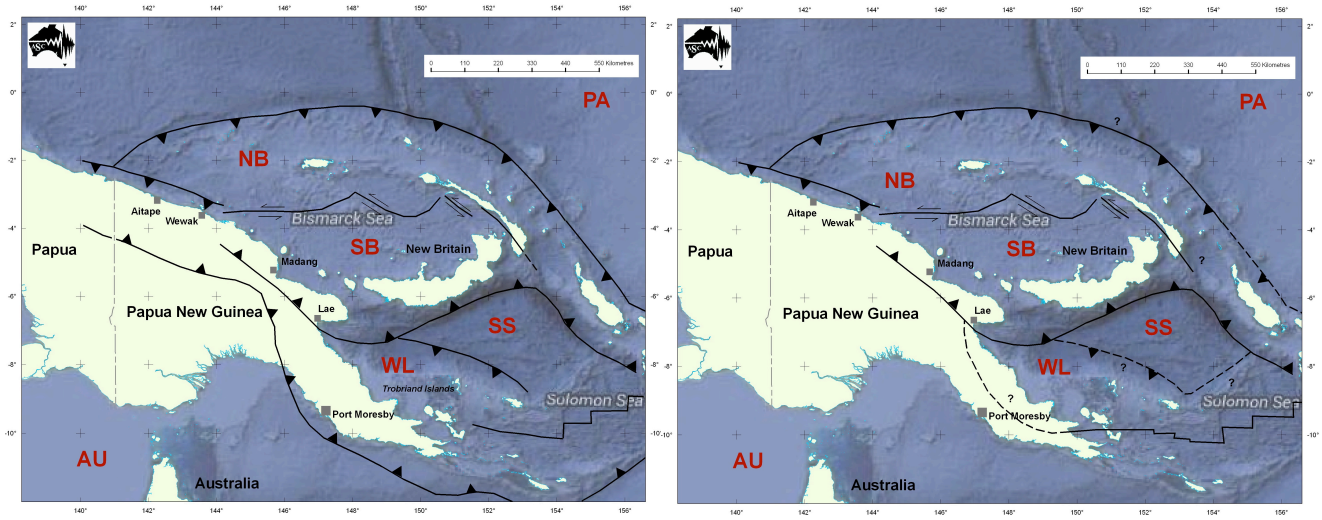

Figure 7.3 Two other postulated geometries (left) by Taylor and others (1991), and Tregoning and others (1998), the latter apparently querying the currency of the Trobriand Trough.

Our own preference is shown in Figure 8, based almost exclusively on the epicentres of the most recent shallow earthquakes, allowing for the large uncertainties in the locations. This is only possible in very active regions. The obvious boundaries of the Australian and Pacific Plates are constructed first, these then help define the smaller plate fragments in the collision zone between them, akin to the fault gouge in the shear zone of a low strain brittle collision. The type of boundary is defined by the earthquake focal mechanisms which also yield the apparent slip directions.

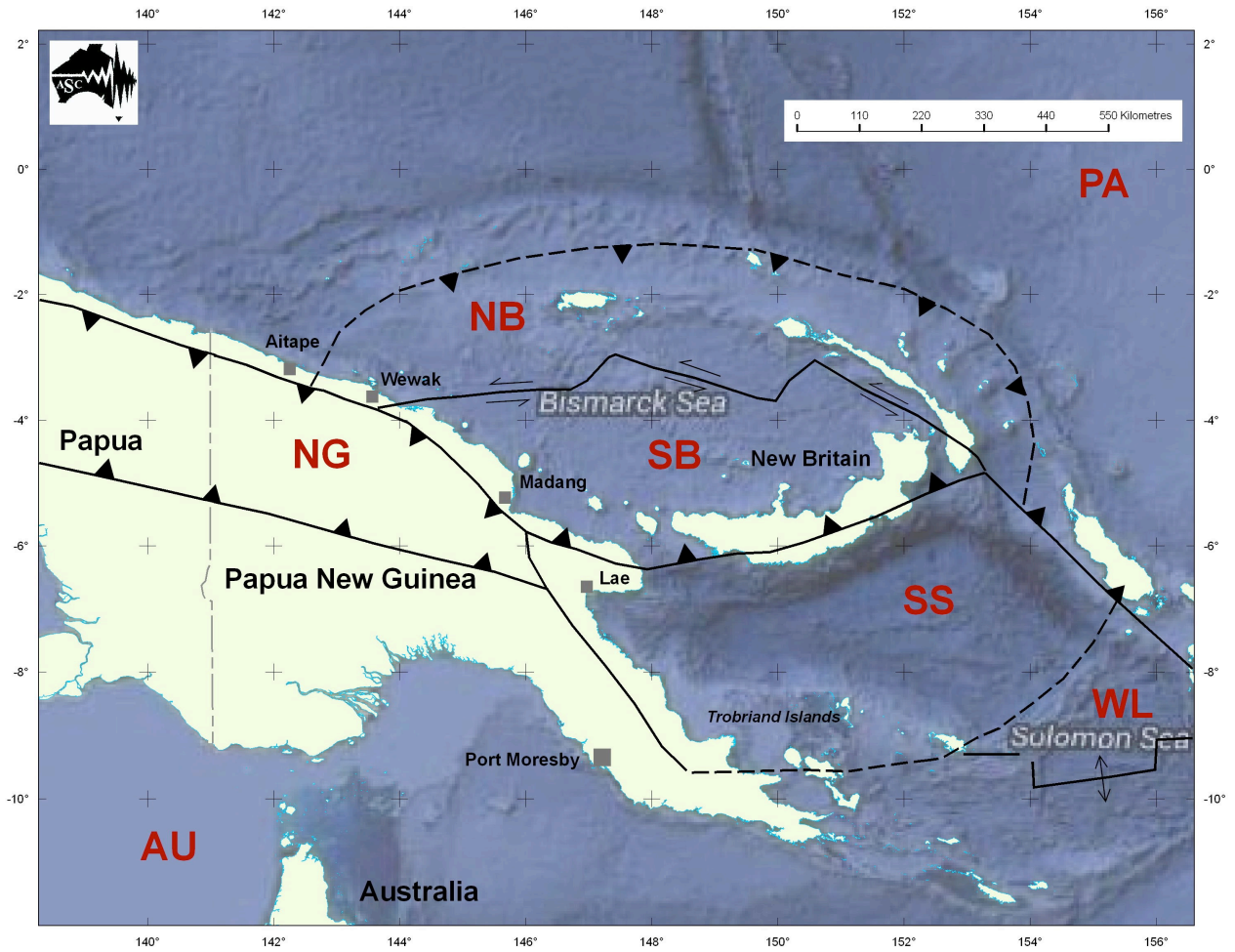

Figure 8. Plate geometry superimposed on the shallow seismicity as proposed in this paper, the Trobriand Trough not active. The Southern Highlands Seismic Zone on the southern boundary of the New Guinea block (NG) links to the Papuan Peninsula and Woodlark Spreading Ridge, the three comprising the north-eastern edge of the Australian Plate.

The 1895 earthquake, it's location and magnitude, the fact that it generated a significant local tsunami implying a shallow rupture and typical tsunamigenic mechanism should then fit into the tectonic model but it doesn't.

DISCUSSION

This study of the 1895 earthquake in the Solomon Sea has reduced the uncertainties in its location and magnitude to a more acceptable level using intensities, with data compiled from German and British colonial reports of the time. This led us to question the activity of the Trobriand Trench and thence the existence of a Woodlark Plate not only on the basis of the lack of more recent seismicity but also on the earthquake mechanism of one of the two large recent earthquake nearby. By our reckoning, the Solomon Plate would extend from the Woodlark spreading ridge in the south right through to the New Britain Trench in the north, and from the Bougainville Trench in the east to the Papuan Peninsula in the west.

The seismological data favour an undivided Solomon Sea Plate. On this interpretation the Trobriand Trough is inactive and the 1895 earthquake would then have been an intraplate earthquake with, consequently, a longer return period than if it had been an interplate event. Earthquake hazard assessments for the Trobriand Islands and region are quite dependent on the model adopted (see Ripper and Letz, 1993) and whether the Trobriand Trough is an active plate boundary or not is critical to the modelled outcome.

REFERENCES

Anton, L. 2009. Analysis of Earthquake Hazard in Papua New Guinea. Monash University thesis submitted for MSc.

Benz, H.M., Herman, Matthew, Tarr, A.C., Hayes, G.P., Furlong, K.P., Villaseñor, Antonio, Dart, R.L., and Rhea, Susan, 2011. Seismicity of the Earth 1900–2010 New Guinea and vicinity: U.S. Geological Survey Open-File Report 2010–1083-H, scale 1:8,000,000.

Bird, P. 2003. An updated digital model of plate boundaries, *Geochemistry Geophysics Geosystems*, *4*(3), 1027, doi:10.1029/2001GC000252.

Brooks, J.A. 1965. Earthquake Activity and Earthquake Risk in Papua New Guinea. BMR Report 74.

Cameron M.L., 2014. Rifting and Subduction in the Papuan Peninsula, Papua New Guinea: The Significance of the Trobriand Trough, the Nubara Strike-Slip Fault, and the Woodlark Rift to the Present Configuration of Papua New Guinea. Ph.D dissertation, Department of Geological Sciences, The University of Alabama, Tuscaloosa, Alabama, USA. http://acumen.lib.ua.edu/content/u0015/0000001/0001515/u0015_0000001_0001515.pdf

Denham, D. 1969. Distribution of Earthquakes in the New Guinea-Solomon Islands Region, JGR, 74, 4290-4299.

Denham, D. 1973. Seismicity, focal mechanisms and the boundaries of the Indian-Australian plate. The Western Pacific: Island Arcs, Marginal Seas, Geochemistry, edited by P.J. Coleman. Nedlands, W.A.: University of Western Australia Press, 35-53.

Denham, D. 1974. Seismicity of the New Guinea/Solomon Islands region, 1968. BMR Record, 169, 1974.

Duda S. 1965. Secular Seismic Energy. Tectonophysics 2,409-452.
Everingham, I.B. 1973. The Major Papua New Guinea Earthquakes beneath Madang (1970) and the North Solomon Sea (1971) Proc. 5th World Conference on Earthquake Engineering, Rome, 1973.
Everingham, I.B. 1974. Large Earthquakes in the New Guinea-Solomon Island area. 1873-1972. Tectonophysics, 23, 323-338.
Everingham, I.B. 1975. Seismological Report on the Madang earthquake of 31 October 1970 and aftershocks. BMR Report 176.
Everingham, I.B. 1975. Faulting associated with the major Solomon Sea earthquakes of 14 and 26 July 1971. J. Geol. Soc. Aust., 22(1), 61-69.
Everingham, I.B. 1977. Preliminary Catalogue of Tsunamis for the New Guinea/Solomon Islands Region. 1768-1972. BMR Report 180, 78p.
Hamilton, W., 1979, Tectonics of the Indonesian region: U.S. Geological Survey Prof. Paper 1078.
Iida, Kumizi, Cox, D.C., and Pararas-Carayannis, G. 1967. Preliminary Catalog of Tsunamis Occurring in the Pacific Ocean, HIG-67-10, Hawaii Institute of Geophysics, University of Hawaii, Honolulu, Hawaii, 275 p. Bibliography to the Preliminary Catalog of Tsunamis Occurring in the Pacific Ocean, December 1967, 27 p.
International Seismological Centre, On-line Bulletin, http://www.isc.ac.uk, Internatl. Seis. Cent., Thatcham, United Kingdom, 2012.
Joku, N. 1999. http://nctr.pmel.noaa.gov/PNG/Upng/N_joku020402/nj_poster.pdf
McCue, K.F. 1982. Seismicity of Papua New Guinea and Neighbouring Region for 1978. GSPNG Report 1982/4.
Macgregor, W. 1897. Annual report on British New Guinea, 1895-1896. Government Printer Brisbane.
NOAA National Geophysical Data Center / World Data Service (NGDC/WDS): Global Significant Earthquake Database. National Geophysical Data Center, NOAA. doi:10.7289/V5TD9V7K
Phillips, C., 1898. The Volcanoes of the Pacific. Transactions and Proceedings of the Royal Society of New Zealand Vol 31, 1898, Art. XLIX.
http://rsnz.natlib.govt.nz/volume/rsnz_31/rsnz_31_00_008250.html.
Ripper, I. D., and Letz, H., 1991. Distribution and origin of large earthquakes in the Papua New Guinea region, 1900-1989. Papua New Guinea Geological Survey Report 91/5.
Ripper, I. D., and Letz, H., 1993. Return periods and probabilities of occurrence of large earthquakes in Papua New Guinea. Papua New Guinea Geological Survey Report 93/1.
NOTE DISCUSSION OF RETURN PERIOD WEST SOLOMON SEA p 52
Ripper, I. D., and Letz, H., 1993. Seismic hazard in Papua New Guinea. In, McGuire, R. K., (Editor),The Practice of Earthquake Hazard Assessment. International Association of Seismology and Physics of the Earth's Interior and European Seismological Commission, 205-209. International Association of Seismology and Physics of the Earth's Interior.
Ripper, I. D., Letz, H., and Moihoi, M., 1999. Felt effects of the 17 July 1998 Sissano Lagoon Earthquakes. Papua New Guinea Geological Survey Report 99/13.
Russian Tsunami Laboratory, Institute of Computational Mathematics and Mathematical Geophysics SB RAS, Tsunami Laboratory, Novosibirsk, Russia Web Encyclopedia on Natural Hazards.

Soloviev, S.L., and Ch.N. Go 1974 A catalogue of tsunamis on the western shore of the Pacific Ocean [dates include 173-1968. Academy of Sciences of the USSR, Nauka Publishing House, Moscow, 439 p. [Canadian Translation of Fisheries and Aquatic Sciences no. 5077, 1984, translation available from Canada Institute for Scientific and Technical Information, National Research Council, Ottawa, Ontario, Canada K1A OS2, 447 p.]. NOAA Ref 414.

Taylor, B.,1979. Bismarck Sea: Evolution of a Back-arc Basin. Geology 7, 171-174.

Tregoning, P., Lambeck, K., Stolz A., Morgan, P., McClusky, S. C., van der Beek, P., McQueen, H. Jackson, R. J. Little, R. P. Laing, A. and Murphy, B. 1998. Estimation of current plate motions in Papua New Guinea from GPS observations J. Geophys, Res, 103, 12,181-12,203, 1998.

ACKNOWLEDGMENT

The Port Moresby Geophysical Observatory has done a remarkable job over many years collecting and disseminating invaluable seismological data and interpretations. Without the efforts of observatory staff, this paper would not have been possible.

ISSN 8755-6839

SCIENCE OF **TSUNAMI HAZARDS**

Journal of Tsunami Society International

Volume 35 **Number 2** **2016**

METHODS OF TSUNAMI DETECTION AND OF POST-TSUNAMI SURVEYS

A. Kurkin[1], V. Belyakov[1], V. Makarov[1)], D. Zeziulin[1], and E. Pelinovsky[1,2,3]

[1] Nizhny Novgorod State Technical University, Nizhny Novgorod, Russia
[2] Institute of Applied Physics, Nizhny Novgorod, Russia
[3] National Research University – Higher School of Economics, Nizhny Novgorod, Russia

ABSTRACT

In our paper we describe some of the methods of the last 25 years which have been used extensively to examine and register tsunami traces - particularly by satellite imaging of coastal zones before and after a tsunami has struck, thus assessing quickly the extent of coastal inundation over large areas without the need of a site visit. Nearly all countries bordering oceans, seas and bodies of water have established digital systems of water level registration in the range of tsunami waves. In this article we describe methods of tsunami detection and runup measurements, some based on our own participation in post-tsunami surveys. Also, we discuss the possibility of using robotic systems to survey tsunami traces in hard-to- reach places.

1. INTRODUCTION

In the 21st century destructive tsunamis caused maximum number of casualties compared to other natural disasters (Pararas-Carayannis, 2006; Bernard et al, 2006; Gusiakov, 2009, 2014). The great earthquake of December 26, 2004, near Sumatra in Indonesia which had moment magnitude (Mw) of 9.3, generated a devastating tsunami in the Indian Ocean, and resulted it the deaths of about 300,000 people (Titov et al, 2005a; Choi et al, 2006). The maximum height of the tsunami wave runup on the shore exceeded 50 meters in certain coastal areas (Kim et al, 2013a). Also, the earthquake of March 11, 2011 off the Island of Honshu in Japan, with moment magnitude of 9.0, triggered another devastating tsunami with the maximum height of about 40 m (Mori et al, 2012; Choi et al, 2012; Kim et al, 2013b; Pararas-Carayannis, G. 2014), resulting also in the destruction of the Fukushima-Daichi nuclear power plant. On the average, tsunamis occur globally almost every month, but only one in ten (about once a year) leads to damage.

On July 9, 1958 a large earthquake along the Fairweather Fault struck Southeastern Alaska. A combination of disturbances triggered by the earthquake triggered a giant rockfall of about 80 million cubic meters off the slopes of a mountain into the Gilbert Inlet of Lituya Bay, Alaska, resulting in the greatest tsunami runup height of 524 m (1,720 feet) on the opposite side (Pararas-Carayannis, 1999; Gusiakov, 2009). Fortunately, since then, national and international tsunami warning services have been created and their effectiveness is constantly improving, especially in predicting distant tsunamis (Titov, 2009). Presently, forecasting tsunamis and their potential impact, has improved considerably and timely-issued warnings are communicated to residents of threatened coastal areas where preparedness includes programs of public education, training of civil defense officials, the designation of safe evacuation zones and other disaster mitigation schemes.

Also, Russia has been impacted in the past by several tsunami disasters. The most destructive tsunami in the post-war history, occurred on November 4-5, 1952 off the coast of Kamchatka and had wave heights of about 10 meters, significantly inflicted destruction at Severo-Kurilsk on Paramushir Island (Kuril Islands) and resulting in the deaths of many of its residents (Gusiakov, 2009). Already in the present century several other large tsunamis occured in the Far East of Russia. In the Kuril Islands, tsunamis on November 15, 2006 and January 13, 2007, had heights of over 10 meters and even had far reaching impact, inflicted damage on the US coast (Laverov et al, 2009). The Nevelsky earthquake of 2007 generated a tsunami of 2 meters in height and was recorded in Sakhalin (Zaitsev et al., 2008).

Tsunamis from distant sources originated from Samoa in 2009 and from Chile in 2010 and were recorded by tide-gauges in Russia (Shevchenko et al, 2013). Finally, the 2011 tsunami from Japan caused cracking of the ice cover in the Kuril Islands (Kaistrenko et al, 2013). Tsunamis have not been limited only to the Far East region of Russia. More than 20 tsunamis were recorded in the Black Sea (Dotsenko, 1995; Yalciner et al, 2004; Papadopoulos, 2011; Zaitsev and Pelinovsky, 2011) and about ten more in the Caspian Sea (Dotsenko et al, 2000). Also tsunami-like phenomena have occurred in inland bodies of waters, such as rivers, lakes and reservoirs (Didenkulova and Pelinovsky, 2006; Torsvik et al, 2010).

A variety of information about tsunamis, the mechanisms of their occurrence and their impact on coastal areas can be found in several books and historical tsunami catalogs (Murty, 1977; Pelinovsky, 1996a; Pararas-Carayannis, 2000; Bryant, 2008; Levin and Nosov, 2009, 2016), as well as on a number of web sites. To understand the physics of tsunamis and the development of methods needed to mitigate their potential damage, it is very important to have reliable data of tsunami terminal characteristics on the coast. After the occurrence of a damaging tsunami, surveys are usually being carried out by national teams using different methodologies to measure inundation and maximum wave heights.

Initial guidelines for the conduct of tsunamis surveys were formulated by scientists at ITIC and at the Joint Institute of Marine and Atmospheric Research (JIMAR) of the University of Hawaii (Loomis, 1981; Curtis, 1982). Earlier versions of guidelines for field surveys were used by international teams after the tsunami of 1992 on Baby Island in Indonesia. Since then, guidelines were further developed with unified standards and specific lists of characteristics that needed to be gathered and documented. Finally, such guidelines for the conduct of tsunamis surveys were subsequently expanded and incorporated in 1998 by ITIC's Director (Pararas-Carayannis, 1998) into IOC manuals and guides #37 (Intergovernmental Oceanographic Commission (of UNESCO), 1998) and subsequently internationally adopted by the member states of the IOC-ITSU Group, including Russia.

Over the years the conduct of such surveys has been summarized in several other scientific publications (Farreras, 1998, 2000; Synolakis and Okal, 2005; Dominey-Howes, 2014). One of the authors of the present paper (EP) participated in international tsunami surveys since 1993 (tsunami in the Sea of Japan), and gained experience which was summarized in Russian in an unpublished document (Pelinovsky, 1996b).

During surveys, accounts of observations from local residents are gathered and measurements are made of the tsunami's, arrival time, the number and polarity of the waves and of the maximum run-up heights. However, as a rule, the managers of the survey get to the stricken area a week or two after the event, when part of the local witnesses have already left the disaster area, and some of the visible traces of the tsunami are lost due to storms, rainfall or recovery work. Nevertheless, the data obtained by each expedition is very useful as the main source for further action to be taken in order to improve tsunami prediction and preparedness for hazard mitigation.

Also over the past 20 years, "non-traditional" methods have been developed for tsunami surveys which enable better planning in studying each tsunami and collection more efficiently of data in remote places. An overview of such methods is the subject of the present article.

2. SATELLITE IMAGERY

Aerial and satellite data is now routinely used to provide timely information about a tsunami, particularly when it is difficult to plan and execute an in situ survey at a remote impact area – given also the shortage of time and funding. During the expedition to the Kuril Islands to document the 1994 Shikotan tsunami (Kaistrenko et al., 2014), for the first time the Russian team used aerial photography, thus allowing the evaluation and determination of the extent of inundation along the entire length of the coastal zone, as well as obtaining an approximation of the runup by using

topographic maps. Such methods were used to collect tsunami data on the Island of Kunashir, subsequently followed by field survey which confirmed the reliability of the images. The United States also had used analysis of satellite imagery of the coast of Japan to assess water runup heights for the 1993 Okushiri tsunami in the Sea of Japan. The images were in good agreement with the data collected by direct measurements of the field investigation (Synolakis and Okal, 2005; Bernard et al, 2006).

These experiences show the validity of quickly obtaining "spatial" information after the occurrence of a tsunami event and the impact of the hazard. Best known are the satellite images which were obtained for the 2004 tsunami in the Indian Ocean, aince it was possible to get before and after imagery from vast areas which was made available via the Internet. Some of the images are unique, such as the picture of the exposed bottom on the west coast of Sri Lanka during the 2004 tsunami (http://www.hanselman.com/blog/content/binary/srilanka_kalutara_beach2_dec26_2004_dg.jpg).

Nowadays satellite images have become an inherent part of surveys of tsunami traces in various parts of the world. Given the impossibility or the difficulty in inspecting the places where a tsunami originated and adversely impacted a coast, makes such images particularly significant. One such example of using such imagery was the earthquake and tsunami of November 15, 2006 near the Simushir Island (uninhabitable now) in the central part of the Kuril Islands, where at that time there were severe ice conditions and it was impossible to organize a field investigation. The satellite image of the neighboring Urup Island of September 6 and November 20, 2006 clearly show the disappearance of grass cover on the coast after the tsunami (Fig. 1). The subsequent expedition in the summer of the next year confirmed the strong impact of the tsunami and the maximum tsunami height was determined to be about 17-20 m (Levin and Nosov, 2016).

Fig. 1. Space images of Urup Island (Kuril Islands) before and after the tsunami of November 15, 2006

For the development of remote sensing of a tsunami on the coast, it is extremely important to understand the mechanisms of forming the images and the photographs, thus a direct inspection is absolutely necessary. The physical reasons for the appearance of features in satellite images are clear, and they are connected with the processes of transporting various substances (sand, salt) on inland, which lead to grass destruction, soil moisture changes and other observations. For example, after the tsunami inundation the shrubbery is killed almost immediately, and the remains of dead wood which stay in seawater are found a few years after a tsunami (Fig. 2). Even the surviving trees preserve the memory of the tsunami in the thickness of the annual rings which appear afterwards. These secondary symptoms were found for the catastrophic Kamchatka tsunami of 1952 (Ivanov and Simonov, 1983). Such data can be used when searching for traces of historic tsunamis in uninhabited regions. The impact of the tsunami inundation on the vegetation cover is very important in the survey of stricken areas, as it allows visual delineation of flooded area and subsequently material evidence of limits of flooding in the form of deposited driftwood, fishing nets, residues or seaweeds. Such evidence reduces the inspection time of the survey, thus allowing additional exploration. In fact, for the 1994 Shikotan tsunami in the Kuril Islands, we collected and have stored samples of seaweeds taken from above and below sea level during, which even now twenty years later, they look different from each other (Fig. 3).

Fig. 2. The part of the coast of Indonesia two years after the tsunami of 1994 (courtesy by EP)

Fig. 3. Samples of grass taken near the flooding of the shore edge during the 1994 Shikotan tsunami, 20 years later (courtesy by EP)

Finally, we wish to mention other applications of space techniques in particular, which are used for the detection and measurement of tsunami waves in the open ocean before making landfall, which allows defining better the tsunami characteristics. Such application first took place during the 2004 tsunami in the Indian Ocean (Smith et al, 2005; Zaitsev et al, 2005). Nowadays the methods of detecting the earthquake and tsunami with the help of GPS - sensors are widely used (Sobolev et al, 2006; Song, 2007).

2. INSTRUMENTAL RECORDING OF TSUNAMIS IN PORTS

Usually tide gauges in the ports are used to measure the sea level changes associated with the tides but also used to register sea level changes due to tsunamis. The older tide gauges, produced a "paper" version of the sea level fluctuations, which is poorly adapted to tsunami recording. As an example of such limitation, we provide the original record of the 1994 Shikotan tsunami in the port of Yuzhno - Kurilsk on the Kunashir Island, Malokurilskoye (Shikotan Island) and in Poronaisk in Sakhalin (Fig . 4), taken from Ivashenko et al (1996). As one can see, the tide-gauge in Yuzhno-Kurilsk broke down during the earthquake, and there appeared an ink stain in the mareograms in Malokurilskoye. The tide gauge resisted destruction and later recorded a tsunami. However, it failed to record the initial stage of the tsunami. Many tide-gauges of this older model stop working during an earthquake and do not record the tsunami. At present there is a transition to a new generation of electronic digital gauges which provide complete records.

These are bottom sensors which record the hydrostatic pressure of passing long period waves, such as tides and tsunamis, and convert the pressure to wave heights. Presently, such a system of buoys named DART (Deep-ocean Assessment and Reporting of Tsunamis) has been deployed in the Pacific Ocean, to specifically record tsunami waves (Mofjeld, 2009). An overview of such tsunami observations in the open ocean has been provided in the literature (Rabinovich, 2014). This system has enabled significant improvements in the prediction of distant tsunami characteristics, because the data on the tsunami in the open ocean can provide an opportunity to solve the inverse problem and define better the tsunami source (Titov et al, 2005b; Titov, 2009).

Russia has also begun to use similar sensors. One of such buoys was installed with the assistance of one of the authors (AK). It uses an autonomous K12 ARV bottom pressure recorder produced by Construction Bureau in Uglich, Russia. This device is shown in Fig. 5. Quartz resonators are used as primary transducers of physical quantities, which ensure low temperature dependence and high accuracy. They work at pressure measuring range (immersion depth) up to 100 m, accuracy of pressure 0.06% and operating temperature in the range of -4 to 40 degrees Celsius. The period of autonomous function of the device is about 6 months and the measurement resolution is 1 sec. The authors used these devices to record the 2007 Nevelsky tsunami and other events (Zaitsev et al, 2008; Shevchenko et al, 2014). At present they are also used to measure wind waves in the coastal zone, including the analysis of the freak waves (Kuznetsov et al., 2014).

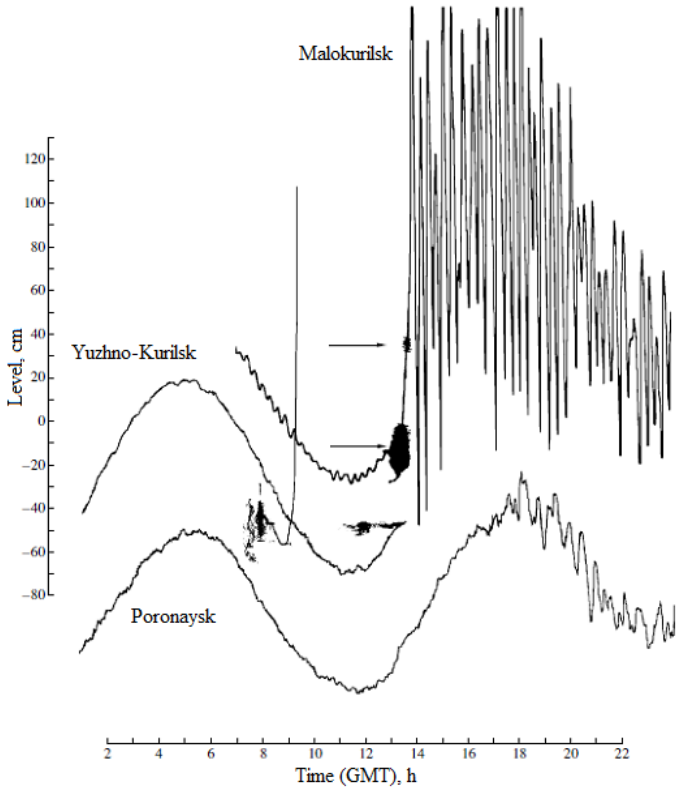

Fig. 4. The tsunami record by tide gauges in Malokurilskoye (Shikotan), Yuzhno-Kurilsk (Kunashir) and Poronaisk (Sakhalin) in 1994.

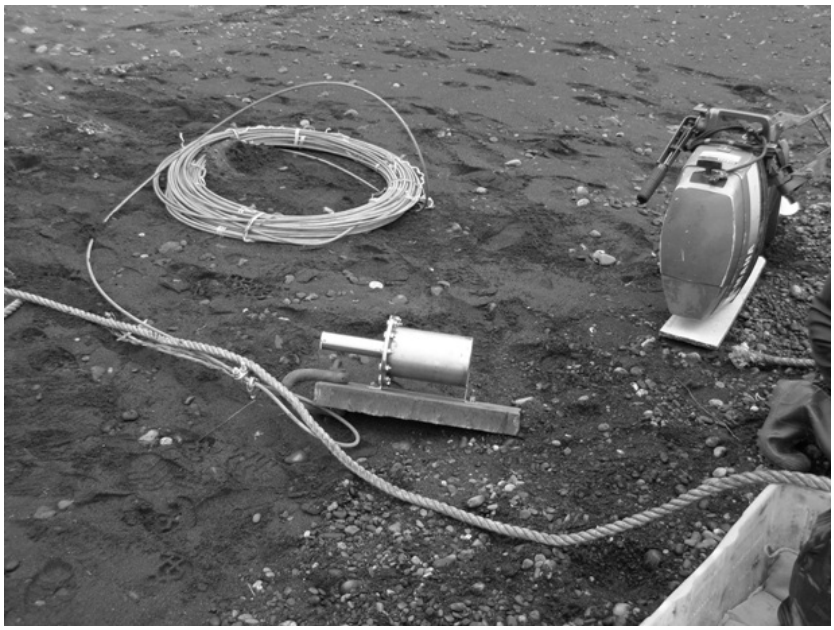

Fig. 5 The bottom pressure sensor

The use of bottom pressure sensors in hydro-physical operational subsystem can significantly enhance the effectiveness of the tsunami warning service. Unfortunately, they have not yet been really used for this purpose in Russia.

3. THE USE OF ROBOTIC SYSTEMS

As it was already mentioned, in some cases the survey of the tsunami traces is connected with the difficulties of visiting certain places. Often, ground subsidence due an earthquake makes many roads and trails impassable. This was the case faced by the authors while surveying the 1994 tsunami on the island of Shikotan near the epicenter of the earthquake, which caused subsidence of about 50 cm. This subsidence of the coastal area and of the seabed is evident on the mareogram (Fig. 4), which shows the change in sea level before and after the tsunami.

On the other hand, during the 2007 Nevelsky tsunami, the bottom of the sea rose and now the sea has receded from Nevelsk (Zaitsev et al, 2008). Such lowering or raising of the seabed and of the sea level is typical of many earthquakes. Shown in Fig. 6, is the location of a village in Indonesia (Island of Sulawesi) in 1996, which subsided by 2 meters due to the 1968 earthquake and destroyed by the tsunami (about 150 people died). Even 30 years later such change of relief is amazing.

Fig. 6. The photograph of a vanished village on the island of Sulawesi (Indonesia) in 1968 as a result of the bottom lowering by 2 m after the earthquake (photo 1996, courtesy EP).

There are many other difficulties in conducting coastal surveys besides the previously-mentioned problems of inaccessibility after an earthquake and tsunami. These include the following:

1. The presence of explosive mines not shown on maps. The survey of the 2004 tsunami along the coastal zone of Sri Lanka was hindered by scattered "old" mines, where for many years a civil war had raged. As a result, the tsunami traces for this part of the island were not measured at all.

2. Radioactive contamination. As it is known, the tsunami of March 11, 2011 off the coast of Japan destroyed the Fukushima-Daichi nuclear power plant and there was extensive coastal radioactive contamination. The radiation prevented the timely examination of the tsunami traces. Thus, data of the tsunami wave heights for this region was received later, when the degree of radioactive contamination was lower.

3. Landslides and avalanches resulting from a main earthquake and its numerous aftershocks in seismically active zones, as well as a tsunami, also hinder the conduct of a survey team . On the basis of personal experience of one of the authors (EP), it was uncomfortable to stand at the foot of a mountain, where coastal flooding by tsunami waves had occurred, while at the same time sufficiently large rocks were sliding down the mountain during aftershocks.

4. Danger to life in remote places. Thus, when surveying the tsunami traces, which occurred after the earthquake of July 17, 1998 on the Papua-New Guinea, many land areas were inaccessible due huge salt-crocodiles inhabiting the island.

5. Malarial and epidemic danger. Dangerous mosquitoes are common in Africa and other tropical locations. To visit these areas a special vaccination is needed. On the basis of the author's own experience, it can be said that working conditions were relatively comfortable on the edge of the shore where the wind did not allow mosquitoes to gather. But the extent of tsunami inland flooding went far away from the coast, where there was no wind, so mosquitoes made it difficult to work.

Based on such difficulties and limitations, it can be concluded that it is a good idea to use robots for the conduct surveys of tsunami and of other natural disasters. The robots can be used to survey the traces of the tsunami, which already happened, as well as to track sea level variations in hard-to- reach places.

Ground-based robotic systems can transport radars, with the help of which it is possible to conduct the measurements of sea wave characteristics in the coastal zone. These systems are ideally suited for long-term deployment, since they make it possible to obtain continuous data, spanning several hundred meters from the coastline and allow studying the coastal areas in the different temporal and spatial scales.

In general, the design of mobile systems is to be determined mainly on the basis of terrestrial band configurations. In designing platforms of this class, the relief of the coastline dissected by bays and coves, must be considered as well as the types of ground base (sandy, sandy- rocky, gravel, silt and rocky).

If working in the Arctic regions, the state of freezing of the components of the shore rocks and their dustiness msut be considered, as well as massive ice inclusions, general ice phenomena and the dynamics of the icy shores. Thus, in creating autonomous mobile systems to monitor coastal zones,

must be based on additional fitting of existing transport and technological complexes and mass-produced ground vehicles by modular attachment - which is not yet very feasible.

More important is the development of special multi-purpose base chassis on which a particular version of the control and information systems can be placed. At the same time there is a serious gap in the field of transport robotics, because there are no domestic mobile systems that fit the task at hand in the market. However, this can be achieved by developing the chassis of modular design with the possibility of re-equipment by various types of propulsion (wheeled, tracked, rotary- screw).

In the research laboratory "Transport Machinery and Transport and Technological Complexes" at the Nizhny Novgorod State Technical University (named after R.Ye. Alekseev) various constructions of all-terrain vehicles have been developed, the examples of which are shown in Fig. 7 (Belyakov and Kulyashov, 2004; Anikin et al, 2012). Vehicles of this type are already being produced by the firm "Plant of all-terrain vehicles" and are used in different geographical and climatic zones. The modular design of the constructions allows adapting the layout of the machine and modifying its individual units in accordance with the requirements of the survey of the disaster areas.

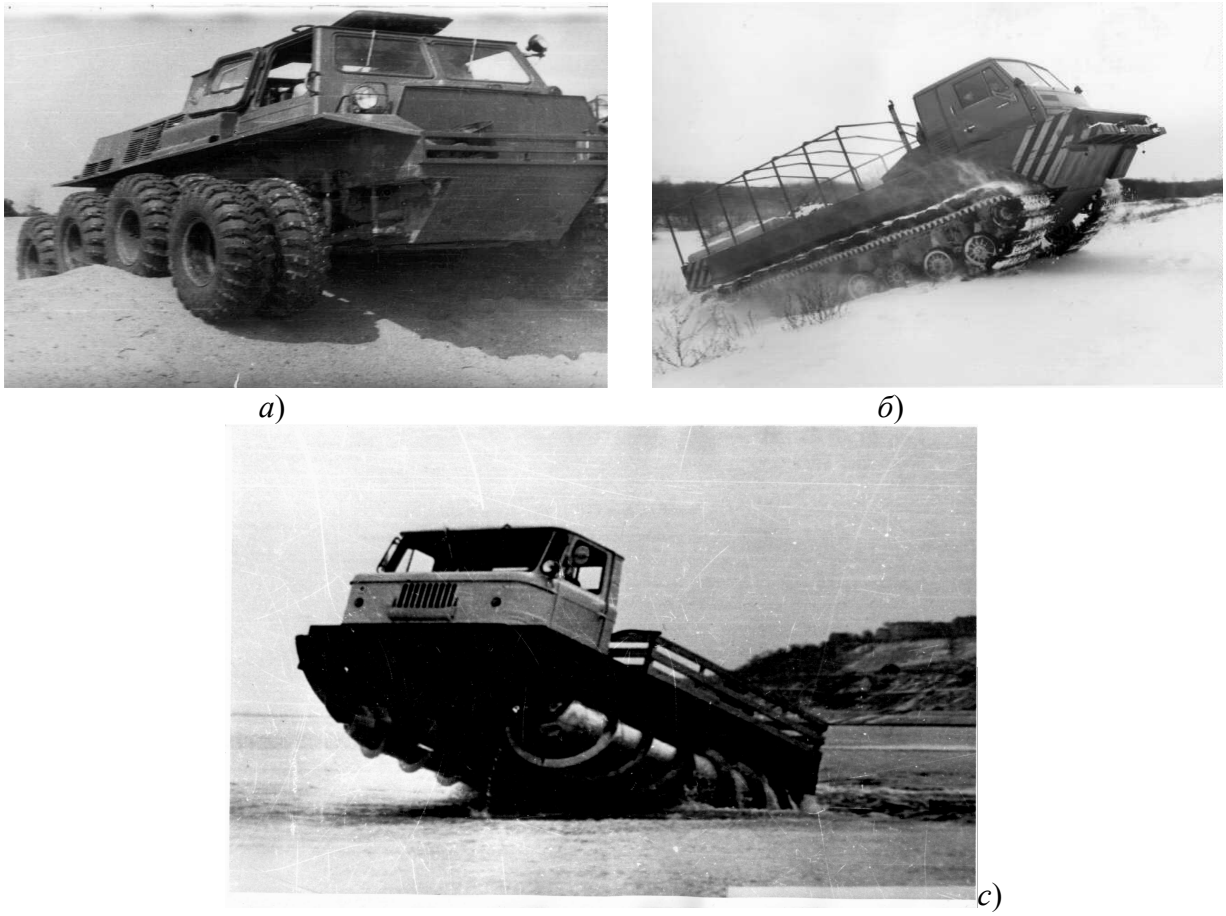

а) *б*) *с*)

Fig. 7. Land - terrain machines with different types of propulsion:
a - wheel; b - tracked; c - rotary-screw

At present, we are developing the autonomous systems of recording parameters of waves and tsunami traces, which can be combined with all-terrain cars of available designs (Kurkin et al, 2015). The selection of gear settings of the robotic complex (Fig. 8) was carried out on the basis of design calculations and of simulation of the interaction of the machine with described areas (Makarov et al, 2014, 2015). In the near future, it is planned use such technology to conduct hydrodynamic measurements on the coast of Sakhalin. Conducting field tests will reveal the development of paossible gaps and will help identify the ways to optimize the structure and functioning of the robotic complex algorithms, as well as the work of the measuring equipment.

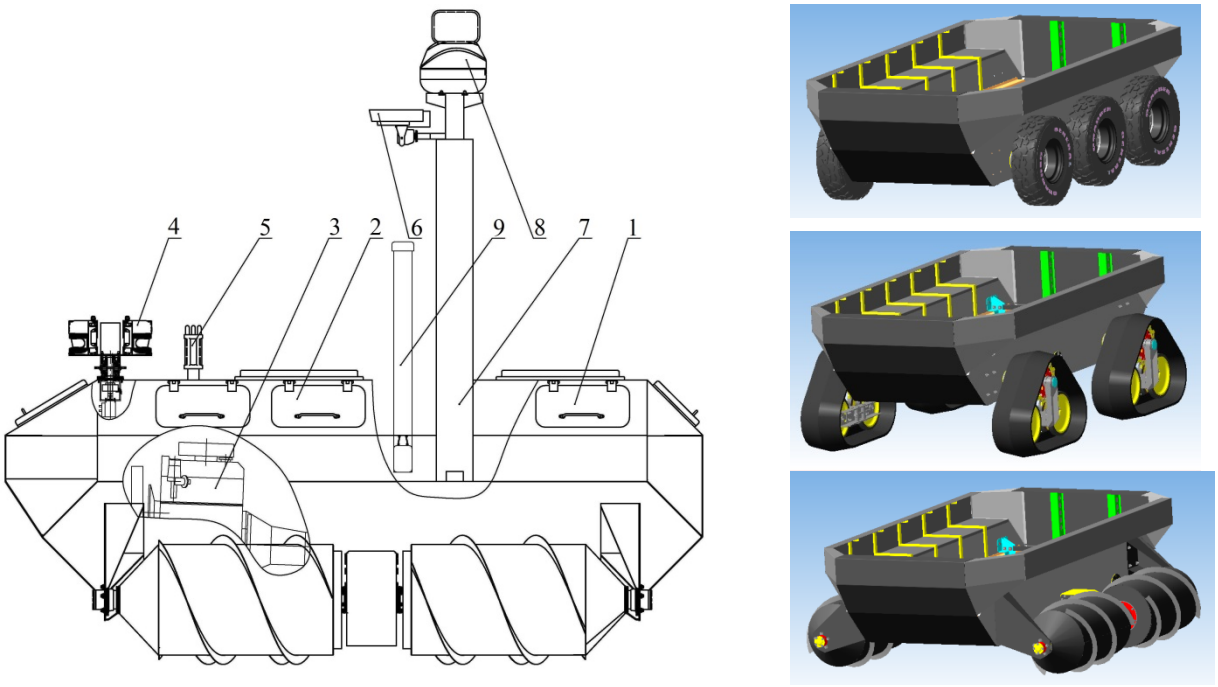

Fig. 8. A general view of the experimental prototype of AMPK with rotary- screw propulsion and mounting options for various types of propulsion:
1 - cross-country vehicle, 2 – superstructure, 3 - engine installation, 4 – lidar setting, 5 – weather station, 6 - camcorder, 7 – Stand, 8 - radar, 9 - antenna

5. Conclusion

In the present article we briefly described the new trends that are being used to survey tsunami traces in recent years. It notes the important role of satellite images, which allow to obtain a picture of flooding on large coastal areas, including hard-to-reach places. The use of bottom pressure sensors for the instrumental registration of a tsunami is extremely important. The need for the use of robotic systems for inspection and registration of tsunami traces in hard-to-reach places is discussed. The constructions of these complexes with good characteristics are given.

Acknowledgements

The results of the given study have been obtained at the Nizhny Novgorod State Technical University (named after R. Alekseev) with financial support for applied scientific research by the Ministry of Education and Science of the Russian Federation Agreement No 14.574.21.0089 (unique identifier of agreement – RFMEFI57414X0089).

REFERENCES

1. Anikin, A.A., Barakhtanov, L.V., Belyakov, V.V., Makarov, V.S. and Maslennikov, V.A. Applied-Research Laboratory of Terrain (snow) Vehicles. On the 50th anniversary (1962 -2012.) Nizhny Novgorod. NNSTU, 2012 272 (in Russian).
2. Belyakov, V.V., and Kulyashov, A.P. All-terrain and technological vehicles. Basic of motion theory. Nizhny Novgorod, TALAM, 2004 (in Russian).
3. Bryant, E. Tsunami – The Underrated Hazard. Springer, 2008.
4. Choi, B.H., Hong, S.J., and Pelinovsky, E. Distribution of runup heights of the December 26, 2004 tsunami in the Indian Ocean. Geophysical Research Letters, 2006, vol. 33, No. 13, L13601.
5. Choi, B.H., Min, B.I., Pelinovsky, E. Tsuji, Y., and Kim, K.O. Comparable analysis of the distribution functions of runup heights of the 1896, 1933 and 2011 Japanese Tsunamis in the Sanriku Area. Natural Hazards and Earth System Sciences, 2012, vol. 12, 1463-1467.
6. Curtis, G.D., 1982. Post-tsunami survey procedures, Joint Institute of Marine and Atmospheric Research Report, University of Hawaii at Manoa, Honolulu Hawaii.
7. Didenkulova, I.I., and Pelinovsky, E.N. Phenomena similar to tsunami in Russian internal basins. Russian Journal of Earth Sciences. 2006, vol. 8, No. 6, ES6002, 9 pages.
8. Dominey-Howes, D., and Dengler, L. International Tsunami Survey Team (ITST) Post-Tsunami Survey Field Guide. 2nd Edition. IOC Manuals and Guides No. 37, Paris: UNESCO 2014
9. Dotsenko, S. F. The Black Sea tsunamis, Izvestiya Atmospheric and Oceanic Physics, 1995, vol. 30(4), 483–489.
10. Dotsenko, S.F., Kuzin, A.P., Levin, B.V., and Solovieva, O.N. Tsunami in the Caspian Sea: seismic sources and features of propagation. Oceanology, 2000, vol. 40, No. 4, 474-482.
11. Farreras, S. Post-tsunami survey field guide. IOS, Manuals and Guides, No. 30. Paris, UNESCO, 1998.
12. Farreras, S. Post-tsunami field survey procedures: An Outline. Natural Hazards 2000, vol. 21, 207–214.
13. Gusiakov, V.K. Tsunami history – recorded. A.Robinson, E.Bernard (Eds.). The Sea, V. 15. Tsunamis. Cambridge, USA: Harvard University Press, 2009, 23-53.
14. Gusiakov, V.K. Strongest tsunamis in the World Ocean and the problem of marine coastal security. Izvestiya, Atmospheric and Oceanic Physics, 2014, vol. 50, No. 5, 435-444.
15. Intrergovernmental Oceanographic Commission (of UNESCO), 1998. Post-Tsunami Survey Field Guide (1st edn), Manuals and Guides #37, (initially compiled by ITIC / G. Pararas-Carayannis). Paris, France.

16. Ivanov, V.V., and Simonov, K.V. Traces of tsunamis in the coastal zone of the Second Kuril Strait. In book: Operative and long-term forecast of tsunamis. DVO AN SSSR. Vladivostok. 1983, 163-170 (in Russian).
17. Ivashenko, A.I., Gusyakov, V.K., Dzhumgaliev, A., Yeh, H., Zhukov, L.D., Zolotukhin, N.D., Kaistrenko. V.M., Kato, L.N., Klochkov, A.A., Korolev, Yu.P., Kruglyakov, A.A., Kulikov, E.A., Kurakin, V.M., Levin. B.V., Pelinovskii, E.N., Poplavskii, A.A., Titov, V.V., Kharlamov, A.A., Khramushin, V.M., and Shelting, E.V. The Shikotan tsunami of October 5, 1994. Transactions (Doklady of the Russian Academy of Sciences) Earth Science Sections, 1996, vol. 348, No. 4, 693-699.
18. Kaistrenko, V., Razjigaeva, N., Kharlamov, A. and Shishkin, A. Manifestation of the 2011 Great Tohoku Tsunami on the Coast of the Kuril Islands: A tsunami with ice. Pure Appl. Geophys., 2013, vol. 170. 1103-1114.
19. Kaistrenko, V., Gusiakov, V., Djumagaliev, V., Dykhan, G., Ivashenko, A., Yeh, H., Kato, L., Klochkov, A., and Pelinovsky, E., 2014. Tsunami manifestation on Shikotan Island based on field survey data. In book: Shikotan earthquake and tsunami on 4(5) October 1994 (Eds: Tikhonov I., Shevchenko G.). Yuzhno-Sakhalinsk: Institute of Marine Geology and Geophysics. 2014. Chapter 10, 59-64.
20. Kim, D.C., Kim, K.O., Choi, B.H., Kim, K.H., and Pelinovsky, E., 2013a. Three-dimensional runup simulation of the 2004 Indian Ocean tsunami at the Lhok Nga Twin Peaks. Journal of Coastal Research, SI, 2013a, 65, 272-277.
21. Kim, D.C., Kim, K.O., Pelinovsky, E., Didenkulova, I., and Choi, B.H., 2013b. Three-dimensional tsunami runup simulation at the Koborinai port, Sanriku coast, Japan. Journal of Coastal Research, SI, 2013b, vol.65, 266-271
22. Kurkin, A., Pelinovsky, E., Tyugin, D., Giniyatullin, A., Kurkina, O., Belyakov, V., Makarov, V., Zeziulin, D., and Kuznetsov, K., 2015. Autonomous robotic system for coastal monitoring. Proc. Twelfth Int. Conf. on the Mediterranean Coastal Environment Medcoast -2015 (06-10 October 2015, Varna, Bulgaria). Ed. E. Ozhan. 933-943.
23. Kuznetsov, K.I., Kurkin, A.A., Pelinovsky, E.N., and Kovalev, P.D., 2014. Features of wind waves at the southern coast of Sakhalin according to bottom-pressure measurements. Izvestiya, Atmospheric and Ocean Physics, 2014, vol. 50, No. 2, 213-220.
24. Laverov, N.P., Lobkovsky, L.I., Levin, B.W., Rabinovich, A.B., Kulikov, E.A., Fine, I.V., and Thomson, R.E., 2009. The Kuril Tsunamis of November 15, 2006, and January 13, 2007: two trans-Pacific events. Doklady Earth Sciences, 2009, vol. 426, No. 4, 658–664.
25. Levin, B., and Nosov, M., 2009. Physics of Tsunamis. Springer, 2009 (1st Ed), 2016 (2d Ed).
26. Loomis H., 1981. Notes on making a tsunami survey, Joint Tsunami Research Effort report, Honolulu, Hawaii, U.S.A.
27. Makarov, V., Kurkin. A., Zeziulin, D. and Belyakov, V., 2015. Development of chassis of robotic system for coastal monitoring. Proc. 13th European Conference of the Int. Society for Terrain-Vehicle Systems, (21-23 October 2015, Rome, Italy), 2015, 524-529.

28. Makarov, V., Zeziulin, D. and Belyakov, V., 2014. Prediction of all-terrain vehicles mobility in snowscape scenes. Proc. 18th Int. Conference of the Int. Society for Terrain-Vehicle Systems, ISTVS (22-25 September 2014, Seoul National University, South Korea), 2014.
29. Mofjeld, H.O., 2009. Tsunami measurements. In: The Sea, Vol. 15, Tsunamis, A.Robinson, E.Bernard (Eds.). USA, Harvard University Press, Cambridge, 2009, 201–235.
30. Mori, N, and Takahashi, T., 2012. The 2011 Tohoku Earthquake Tsunami Joint Survey Group. Nationalwide post event survey and analysis of the 2011 Tohoku Earthquake Tsunami. Coast. Eng. J., 2012, vol. 54, 1-27.
31. Murty, T.S. , 1977. Seismic Sea Waves – Tsunamis. Ottawa, Canada, 1977.
32. Pararas-Carayannis, G., 1999. Analysis of mechanism of tsunami generation in Lituya Bay. Science of Tsunami Hazards 17(3): 193-206. Also, The Mega-Tsunami of July 9, 1958 in Lituya Bay, Alaska - Analysis of Mechanism http://www.drgeorgepc.com/Tsunami1958LituyaB.html
33. Pararas-Caraynnis, G., 2000. The Big One. Aston Forbes Press, ISBN: 0-9709725-0-4.
34. Pararas-Carayannis, G., 2006. Disaster risk assessment - Overview of basic principles and methodology**.** Natural Disaster Risks, 2006, No. 3, 17-73.
35. Pararas-Carayannis, G., 2014. The Great Tohoku-Oki Earthquake and Tsunami of March 11, 2011 in Japan: A critical Review and Evaluation of theTsunami Source Mechanism. Pure and Applied Geophysics, 171 (2014, 3257-3278 DOI 10.1007.
36. Pelinovsky, E.N. 1996a Tsunami Wave Hydrodynamics. Institute Applied Physics Press, Nizhny Novgorod. 1996a (in Russian).
37. Pelinovsky E. N., 1996b. International tsunami expeditions. Vestnik RFFI (Herald of Russian Fund for Basic Research), 1996b, No 5, 26 – 30 (in Russian).
38. Papadopoulos, G.A., Diakogianni, G., Fokaefs, A., and Ranguelov, B., 2011. Tsunami hazard in the Black Sea and the Azov Sea: a new tsunami catalogue Nat. Hazards Earth Syst. Sci., 2011, vol. 11, 945–963.
39. Rabinovich, A.B., 2014. Tsunami observations in the open ocean. Izvestiya, Atmospheric and Oceanic Physics, 2014, vol. 50, No. 5, 445–458.
40. Shevchenko, G., Ivelskaya, T., Loskutov, A., and Shishkin, A., 2013. The 2009 Samoan and 2010 Chilean tsunamis recorded on the Pacific coast of Russia. Pure Appl. Geophys. 2013, vol. 170, 1511-1527.
41. Shevchenko, G.V., Ivelskaya, T.N., and Loskutov, A.V., 2014. Instrumental measurements of 2009-2011 tsunamis on the Russian Pacific Coast. Izvestiya, Atmospheric and Oceanic Physics, 2014, vol. 50, No. 5, 459-473.
42. Smith, W.H.F, Scharroo, R., Titov, V.V., Arcas, D., Arbic, B.K.. 2005. Satellite altimeters measure tsunami. Oceanography, 2005, vol. 18, 10-12.
43. Sobolev, S. V., Babeyko, A.Y., Wang, R., Hoechner, A., Galas, R., Rothacher, M., Sein, D.V., Schroter, J., Lauterjung, J., and Subarya, C., 2007. Tsunami early warning using GPS-Shield arrays, J. Geophys. Res., 2007, 112, B08415
44. Song, Y.T., 2007. Detecting tsunami genesis and scales directly from coastal GPS stations, Geophys. Res. Lett., 2007, 34, L19602
45. Synolakis, C.E., and Okal E.A., 2005. 1992−2002: Perspective on decade of post-tsunami surveys. Tsunamis: Case Studies and Recent Developments (Ed. K. Satake), Springer, 2005, 1-29.

46. Titov, V., Rabinovich, A., Mofjeld, H., Thomson, R, and Gonzalez, F., 2005a. The global reach of the 26 December, 2004 Sumatra tsunami, Science, 2005a, 309, P. 2045–2048.
47. Titov, V.V., González, F.I., Bernard, E.N., Eble, M.C., Mofjeld, H.O., Newman, J.C., and Venturato, A.J., 2005b. Real-time tsunami forecasting: Challenges and solutions. Nat. Hazards, vol. 35(1), 2005b, 41–58.
48. Titov, V.V., 2009. Tsunami forecasting. In: The Sea, Vol.15, Tsunamis, Eds.: A. Robinson, E. Bernard, Harvard Univ. Press, Cambridge. 2009, 371–400.
49. Torsvik, T., Paris, R., Didenkulova, I., Pelinovsky, E., Belousov, A., and Belousova, M., 2010. Numerical simulation of tsunami event during the 1996 volcanic eruption in Karymskoe lake, Kamchatka, Russia. Natural Hazards and Earth System Sciences, 2010, vol. 10, 2359-2369.
50. Yalciner, A., Pelinovsky, E., Talipova, T., Kurkin, A., Kozelkov, A., and Zaitsev, A. 2004. Tsunamis in the Black Sea: comparison of the historical, instrumental and numerical data. J. Geophys. Research, 2004, vol. 109, No. C12, C12023.
51. Wübbold, F., Hentschel, M., Vousdoukas, M., and Wagner, B., 2012. Application of an autonomous robot for the collection of nearshore topographic and hydrodynamic measurements. Coastal Engineering Proceedings, 2012, vol. 33, management. 53 (ISBN 978-0-9896611-1-9).
52. Zaitsev, A.I., Kurkin, A.A., Levin, B.V., Pelinovsky, E.N., Yalciner, A., Troitskaya, Yu.I., and Ermakov, S.A., 2005. Numerical simulation of catastrophic tsunami propagation in the Indian Ocean. Doklady Earth Sciences, 2005, vol. 402, No. 4, 614-618.
53. Zaitsev, A.I., Kovalev, D.P., Kurkin, A.A., Levin, B.W., Pelinovsky, E.N., Chernov, A.G., and Yalciner, A., 2008. The Nevelsk tsunami on August 2, 2007: Instrumental data and numerical modeling. Doklady Earth Sciences, 2008, vol. 421, No. 1, 867-870.
54. Zaitsev, A.I., and Pelinovsky, E.N., 2011. Forecasting of tsunami wave heights at the Russian Coast of the Black Sea. Oceanology, 2011, vol. 51, No. 6, 907-915.

ISSN 8755-6839

SCIENCE OF **TSUNAMI HAZARDS**

Journal of Tsunami Society International

Volume 35 **Number 2** **2016**

TSUNAMI DISPERSION SENSITIVITY TO SEISMIC SOURCE PARAMETERS

Oleg Igorevich Gusev, Sofya Alexandrovna Beisel

Institute of Computational Technologies of SB RAS, 6 Acad. Lavrentjev Avenue, 630090 Novosibirsk, Russia

ABSTRACT

The study focuses on the sensitivity of frequency dispersion effects to the form of initial surface elevation of seismic tsunami source. We vary such parameters of the source as rupture depth, dip-angle and rake-angle. Some variations in magnitude and strike angle are considered. The fully nonlinear dispersive model on a rotating sphere is used for wave propagation simulations. The main feature of the algorithm is the splitting of initial system on two subproblems of elliptic and hyperbolic type, which allows implementation of well-suitable numerical methods for them. The dispersive effects are estimated through differences between computations with the dispersive and nondispersive models. We consider an idealized test with a constant depth, a model basin for near-field tsunami simulations and a realistic scenario. Our computations show that the dispersion effects are strongly sensitive to the rupture depth and the dip-angle variations. Waves generated by sources with lager magnitude may be even more affected by dispersion.

Keywords: *seismic source, tsunami propagation, frequency dispersion, fully nonlinear dispersive model, rotating sphere, numerical modelling.*

Vol. 35, No. 2, Page 84, (2016)

1. INTRODUCTION

Nonlinear dispersive (NLD) equations are being investigated over than fifty years and have been realized in such tsunami models as TUNAMI-N2-NUS (Dao and Tkalich 2007), FUNWAVE (Kirby et al. 2013), COULWAVE (Lynett and Liu 2002) and GloBouss (Lovholt et al. 2008). However, most of tsunami studies are based on computations with using of nondispersive shallow water equations, realized, for example, in such models as MGC (Shokin et al. 2008, Kosykh et al. 2013), MOST (Titov and Synolakis 1995) and other (see also review in Horrillo et al. 2015 and references therein). The question of the importance of dispersion in tsunami problems is still being discussed by the researchers (see the citations above). We note study (Glimsdal et al. 2013) which is devoted to this question and includes numerical results for ten historical and potential tsunamis. Its authors introduced the parameter called "normalized dispersion time",

$$\tau = \frac{6 h_{depth}^{\ 2} L_{dist}}{\lambda_{wave}^{\ 3}}, \qquad (1)$$

which corresponds to the dispersion significance. Here h_{depth} is characteristic depth, λ_{wave} is characteristic wavelength, L_{dist} is propagation distance. They estimated that "the effect of dispersion is small for $\tau < 0.01$, while it generally becomes significant for $\tau > 0.1$". Similar parameters were earlier proposed in (Kajiura 1963; Pelinovsky 1996).

The main difficulty of this estimation usage is the determination of the wavelength for the real source. Note that in (1) the wavelength is in the power of three, meaning that it is the most significant parameter. Mostly, researchers utilize Okada model (Gusiakov 1978; Okada 1985) for seismic source simulations and identify λ_{wave} as the minimal source extension. However, there are several parameters responsible for the form of the initial surface elevation. The sensitivity of the dispersion effects to variations of these parameters seems to be not investigated, and so it serves as the subject of the present study.

Most of the NLD models mentioned above are based on the equations on a rotating sphere because the effects of dispersion become stronger at large propagation distances, where effects of sphericity and rotation of the Earth should also be taken into account. In the present work, we use a fully nonlinear dispersive (FNLD) model (Fedotova and Khakimzyanov 2010) on a rotating sphere based on depth-averaged velocity. The main feature of the employed numerical algorithm lies in the splitting (Gusev and Khakimzyanov 2015) of the FNLD equations into two subproblems of elliptic and hyperbolic type. Such approach allows utilizing well-suitable methods for the subproblems.

This paper is organized as follows. In the next section, we summarize main features of the Okada model and the FNLD propagation model. The importance of frequency dispersion is then discussed through the numerical results obtained with the FNLD model and the nondispersive nonlinear shallow water (NLSW) model. We consider an idealized test with a constant depth, the

model basin “Wash-tube” for near-field tsunami computations and a realistic scenario.

2. TSUNAMI MODEL DESCRIPTION

2.1. Seismic source model

In our computations, seismic tsunami sources are generated according to the standard method (Okada 1985), in which the seafloor deformation is computed in a homogeneous elastic half-space with a planar dislocation and then specified on the free surface as an initial condition, with zero initial flow velocity. Such internal dislocation source is characterized by the following parameters: the source centroid location, the width and the length of the fault, W and L, respectively, the depth of the upper bound of the fault, H_{rupt}, the fault slip value, D_0, the angle between the fault and a horizontal plane (dip-angle), δ, the fault direction relative to north (strike-angle), θ_s, and the slip direction (rake-angle), λ_r. We use program complex MGC for computation of initial surface disturbance of seismic source.

2.2. Propagation model

Consider the sphere of radius R rotating with the constant velocity Ω around the axis Oz of the fixed Cartesian system $Oxyz$. The coordinate plane Oxy of the latter coincides with the equatorial plane of the sphere. For water flow description the rotating coordinate system $O\lambda\theta r$ is used, where λ is the longitude counted in the direction of the rotation from a certain meridian $(0 \le \lambda \le 2\pi)$, θ is the addition to the latitude (we assume $\theta_0 \le \theta \le \pi - \theta_0$ with a small angle $\theta_0 = const > 0$, i.e. poles are excluded from the consideration), r is the radial distance from the sphere center.

The Newtonian attractive force $\vec{g}$ acts on liquid particles towards the center of the sphere. The thickness of the water layer $H = \eta + h > 0$ is assumed to be small compared to the radius of the sphere, so the values of $g = |\vec{g}|$ and of water density ρ are assumed to be constant throughout the liquid layer bounded below by the impermeable moving bottom, h, and above by the free surface, η:

$$r = R - h(\lambda,\theta,t), \qquad r = R + \eta(\lambda,\theta,t). \tag{2}$$

For waves propagation simulation we use fully nonlinear dispersive (FNLD) model on a rotating sphere (Fedotova and Khakimzyanov 2010)

$$\begin{aligned} &H_t + \frac{1}{R\sin\theta}\left((Hu)_\lambda + (Hv\sin\theta)_\theta\right) = 0, \\ &u_t + \frac{1}{R\sin\theta}uu_\lambda + \frac{1}{R}vu_\theta + \frac{1}{R\sin\theta}g\eta_\lambda = \frac{1}{R\sin\theta}\frac{\varphi_\lambda - \psi h_\lambda}{H} - \frac{uv}{R}\cot\theta - fv \end{aligned} \tag{3}$$

$$v_t + \frac{1}{R\sin\theta} u v_\lambda + \frac{1}{R} v v_\theta + \frac{1}{R} g\eta_\theta = \frac{1}{R}\frac{\varphi_\theta - \psi h_\theta}{H} + \frac{u^2}{R}\cot\theta + f u + \Omega^2 R\sin\theta\cos\theta.$$

Here the symbols u and v denote the physical components of the velocity vector ($u = Rc^1\sin\theta$, $v = Rc^2$, $c^1 = \frac{d\lambda}{dt}$, $c^2 = \frac{d\theta}{dt}$), and $f = 2\Omega\cos\theta$ is the Coriolis parameter, expressed in terms of latitude's addition θ.

The functions φ and ψ included in the right sides of equations (3) are the dispersive components of the depth-integrated pressure p and the pressure p_0 at the bottom respectively,

$p = gH^2 - \varphi$, $p_0 = gH - \psi$.

Dispersive additives are expressed by the following formulas:

$$\varphi = \frac{H^3}{3} Q_1 + \frac{H^2}{2} Q_2, \qquad \psi = \frac{H^2}{2} Q_1 + H Q_2,$$

where

$$Q_1 = D(\nabla\cdot\vec{c}) - (\nabla\cdot\vec{c})^2, \qquad Q_2 = D^2 h, \ \vec{n} = (\tilde{n}^1, c^2),$$

$$D = \frac{\partial}{\partial t} + \vec{c}\cdot\nabla, \qquad \nabla = \left(\frac{\partial}{\partial\lambda}, \frac{\partial}{\partial\theta}\right),$$

$$\vec{c}\cdot\nabla = c^1\frac{\partial}{\partial\lambda} + c^2\frac{\partial}{\partial\theta}, \qquad \nabla\cdot\vec{c} = c^1_\lambda + \frac{1}{J}\left(J c^2\right)_\theta, \qquad J = -R\sin^2\theta.$$

In detail

$$Q_1 = (\nabla\cdot\vec{c})_t + \frac{1}{R\sin\theta}\left(u(\nabla\cdot\vec{c})_\lambda + v(\nabla\cdot\vec{c})_\theta\sin\theta\right) - (\nabla\cdot\vec{c})^2,$$

$$Q_2 = (Dh)_t + \frac{1}{R\sin\theta}\left(u(Dh)_\lambda + v(Dh)_\theta\sin\theta\right),$$

$$\nabla\cdot\vec{c} = \frac{1}{R\sin\theta}\left(u_\lambda + (v\sin\theta)_\theta\right), \qquad Dh = h_t + \frac{1}{R\sin\theta}\left(uh_\lambda + vh_\theta\sin\theta\right).$$

FNLD model (3) is called "fully" because it is derived without the assumption on the smallness of wave amplitudes, and all the nonlinear terms associated with dispersion are stored. So, one can use it for calculation of the surface wave propagation over an uneven bottom both in a deep water and in a coastal zone. The FNLD model allows also to simulate the wave generation by the long-time shifts of bottom fragments, which extends the range of problems that can be solved within the framework of the known NLD models on a sphere (Dao and Tkalich 2007; Lovholt at al. 2008; Kirby et al. 2013).

Moreover, FNLD model can be written in the quasi conservative form of mass and momentum balances (Fedotova and Khakimzyanov 2014), and it has the balance equation of the total energy, agreed with the similar equation of the 3D-model, which not only confirms the physical consistency of the model, but also allows an additional control of the calculations.

System (3) is not a system of Cauchy–Kovalevskaya type because the equations of motion contain the mixed third-order derivatives of the velocity vector components with respect to time and space. A direct approximation of the derivatives leads to a complex problem, which is difficult to solve. In the case of a plane geometry, it turned out fruitful (Gusev 2014; Khakimzyanov et al. 2015) to split the original system on the scalar equation of elliptic type and the system of hyperbolic equations. In the present work, we use this approach to equations (3) on a rotating sphere.

The splitting of system (3) results in the hyperbolic equations

$$
\begin{aligned}
&\left(HR\sin\theta\right)_t + \left(Hu_\lambda\right) + \left(Hv\sin\theta\right)_\theta = 0,\\
&\left(HuR\sin\theta\right)_t + \left(Hu^2 + g\frac{H^2}{2}\right)_\lambda + \left(Huv\right)_\theta = gHh_\lambda - Huv\cos\theta - fvHR\sin\theta + \varphi_\lambda - \psi h_\lambda, \qquad (4)\\
&\left(HvR\sin\theta\right)_t + \left(Huv\right)_\lambda + \left(Hv^2 + g\frac{H^2}{2}\right)_\theta = gHh_\theta\sin\theta + g\frac{H^2}{2}\cos\theta + Hu^2\cos\theta +\\
&\qquad + fuHR\sin\theta + \left(\varphi_\theta - \psi h_\theta\right)\sin\theta + \Omega^2 HR^2\sin^2\theta\cos\theta,
\end{aligned}
$$

with first-order derivatives only, and the uniformly elliptic equation for the dispersive component φ

$$
\begin{aligned}
&\frac{1}{\sin\theta}\left(\frac{\varphi_\lambda}{H} - \frac{h_\lambda}{H}\frac{\nabla h\cdot\nabla\varphi}{r}\right)_\lambda + \left(\frac{\varphi_\theta}{H} - \left(\frac{h_\theta}{H}\frac{\nabla h\cdot\nabla\varphi}{r}\right)\sin\theta\right)_\theta -\\
&\qquad - 6\varphi\left(\frac{1}{\sin\theta}\left(\frac{h_\lambda}{H^2 r}\right)_\lambda + \left(\frac{h_\theta}{H^2 r}\sin\theta\right)_\theta + \frac{2}{H^3}\frac{r-3}{r}R^2\sin\theta\right) = F,
\end{aligned}
\qquad (5)
$$

where

$$
\begin{aligned}
F = &\left(\frac{1}{\sin\theta}\left(g\eta_\lambda + \frac{Q}{r}h_\lambda - a_1\right)\right)_\lambda + \left(\sin\theta\left(g\eta_\theta + \frac{Q}{r}h_\theta - a_2\right)\right)_\theta - 6\frac{Q}{Hr}R^2\sin\theta -\\
&- \left(v^2\cos\theta\right)_\theta - 2(uv)_\lambda\cot\theta + \frac{2}{\sin\theta}\left(u_\lambda + \left(v\sin\theta\right)_\theta\right)^2 - 2\left(u_\lambda v_\theta - u_\theta v_\lambda\right),\\
\nabla\varphi\cdot\nabla h = &\frac{1}{R^2}\left(\frac{\varphi_\lambda h_\lambda}{\sin^2\theta} + \varphi_\theta h_\theta\right),
\end{aligned}
$$

$$Q = -g\nabla\eta\cdot\nabla h + \frac{1}{R^2\sin\theta}\left(\frac{u^2}{\sin\theta}h_{\lambda\lambda} + 2uvh_{\lambda\theta} + v^2 h_{\theta\theta}\sin\theta\right) + h_{tt} +$$

$$+ 2\left(\frac{u}{R\sin\theta}h_{\lambda t} + \frac{v}{R}h_{\theta t}\right) + \frac{a_1 h_\lambda}{R^2\sin^2\theta} + \frac{a_2 h_\theta}{R^2},$$

$$a_1 = -2uv\cos\theta - fvR\sin\theta, \qquad a_2 = u^2\cot\theta + fuR + \Omega^2 R^2\sin\theta\cos\theta.$$

Note that neither the left nor the right part of (5) does not contain time derivatives of the dependent variables H, u and v. Values of the dispersive component ψ are calculated from the expression

$$\psi = \frac{1}{r}\left(\frac{6\varphi}{H} + HQ + \nabla\varphi\cdot\nabla h\right).$$

Supposing $\varphi = \psi \equiv 0$, one obtain NLSW model (Cherevko and Chupakhin 2009) on a rotating sphere.

We note that the still water level doesn't have a spherical form, and can be described by the equation $r = R + \eta_{00}(\theta)$, where

$$\eta_{00}(\theta) = \frac{1}{2g}\Omega^2 R^2\sin^2\theta + const.$$

It is natural to measure the free surface and the depth not as deviations (2) from a sphere surface, but as the deviations $\bar{\eta}$ and $\bar{h}$ from the still water level. These functions are connected with (2) as

$$\bar{\eta} = \eta - \eta_{00}, \qquad \bar{h} = h + \eta_{00}.$$

We construct a numerical algorithm for extended system (4), (5) as alternate solving of the hyperbolic and the elliptic subproblems on each time step. Such approach allows us to use well-suitable methods for them. The hyperbolic system is implemented using a second-order predictor-corrector scheme, and the elliptic equation is solved by integro-interpolation and SOR methods. Totally, we develop the algorithm of second-order approximation in space and time. For a more detailed description of the model, see (Gusev and Khakimzyanov 2015). Some properties of the algorithm, such as correctness, stability, numerical dispersion and dissipation, were investigated in studies (Gusev 2012; Fedotova et al. 2015). Considering the sphericity and rotation effects are small in some tests presented below, we use also a plane analogue of the model (Gusev 2014; Khakimzyanov et al. 2015). In the next section, we estimate frequency dispersion influence comparing the numerical solutions obtained with the FNLD and the NLSW models.

RESULTS OF COMPUTATIONS

2.3. Flat bottom test

We first demonstrate the motivation of the present work in the following test. The computational domain

$$\Omega^d = \{(x, y):\ x \in [Lx_1 : Lx_2]\ \ y \in [Ly_1 : Ly_2]\}$$

in Cartesian coordinates lies from $Lx_1 = -1100$ km to $Lx_2 = 1100$ km in the Ox direction, and the same in the Oy direction, $Ly_1 = -1100$ km, $Ly_2 = 1100$ km. The main idealization of this test consists in assuming that the water depth $\bar{h}$ is constant, $\bar{h} \equiv 4$ km. A seismic sources obtained with the Okada model were disposed in the center of the domain. Here we consider four cases of the source: with magnitude $Mw = 7.8$ and $Mw = 9.0$, and with rupture depth $H_{rupt} = 10$ km and $H_{rupt} = 50$ km (Fig. 1). Note that decreasing of the rupture depth makes the initial free surface steeper.

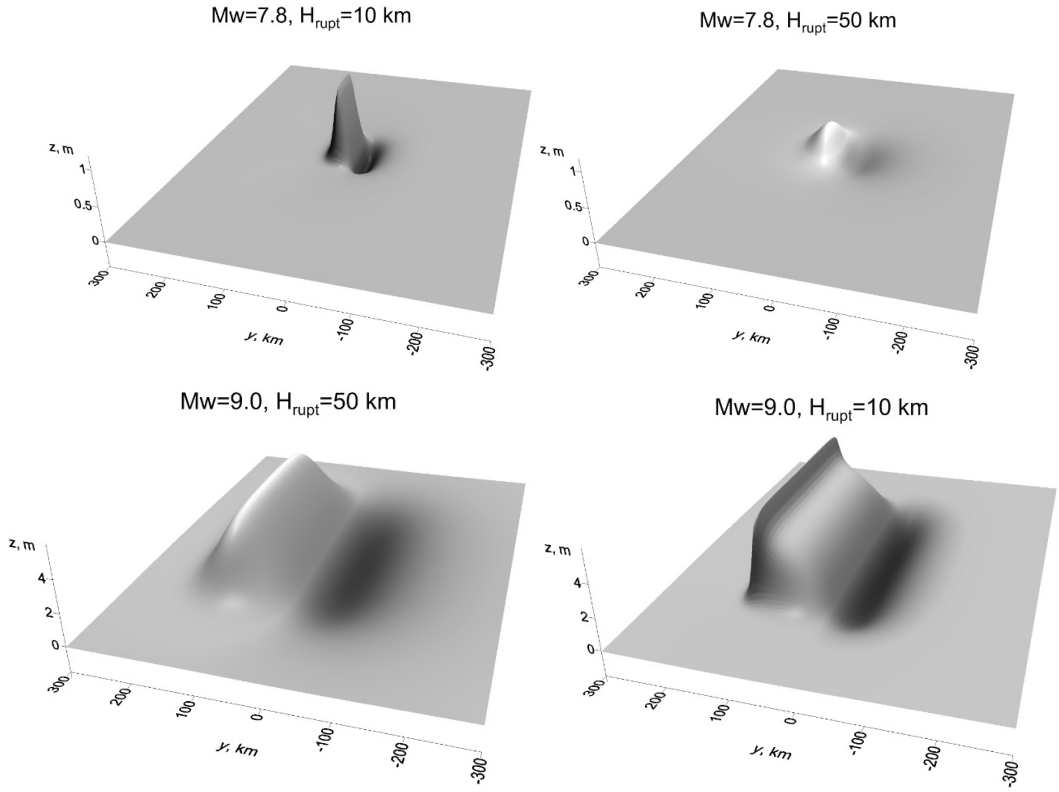

Figure 1. Initial free surface profiles for the flat bottom test

For the computations, we utilize an uniform grid

$$\Omega_h^d = \{(j_1, j_2): \ j_1 = 0,...,N_1, \ \ j_2 = 0,...,N_2\}.$$

The results presented here were computed using the grid $N_1 \times N_2 = 2400 \times 2400$ which corresponds to the resolution $\Delta x = \Delta y \approx 917$ m (30-second grid in spherical case). The convergence of the obtained solutions have been checked using finer grids (with $\Delta x = \Delta y \approx 460$ m).

The dispersion influence for the proposed sources is illustrated in Fig. 2.

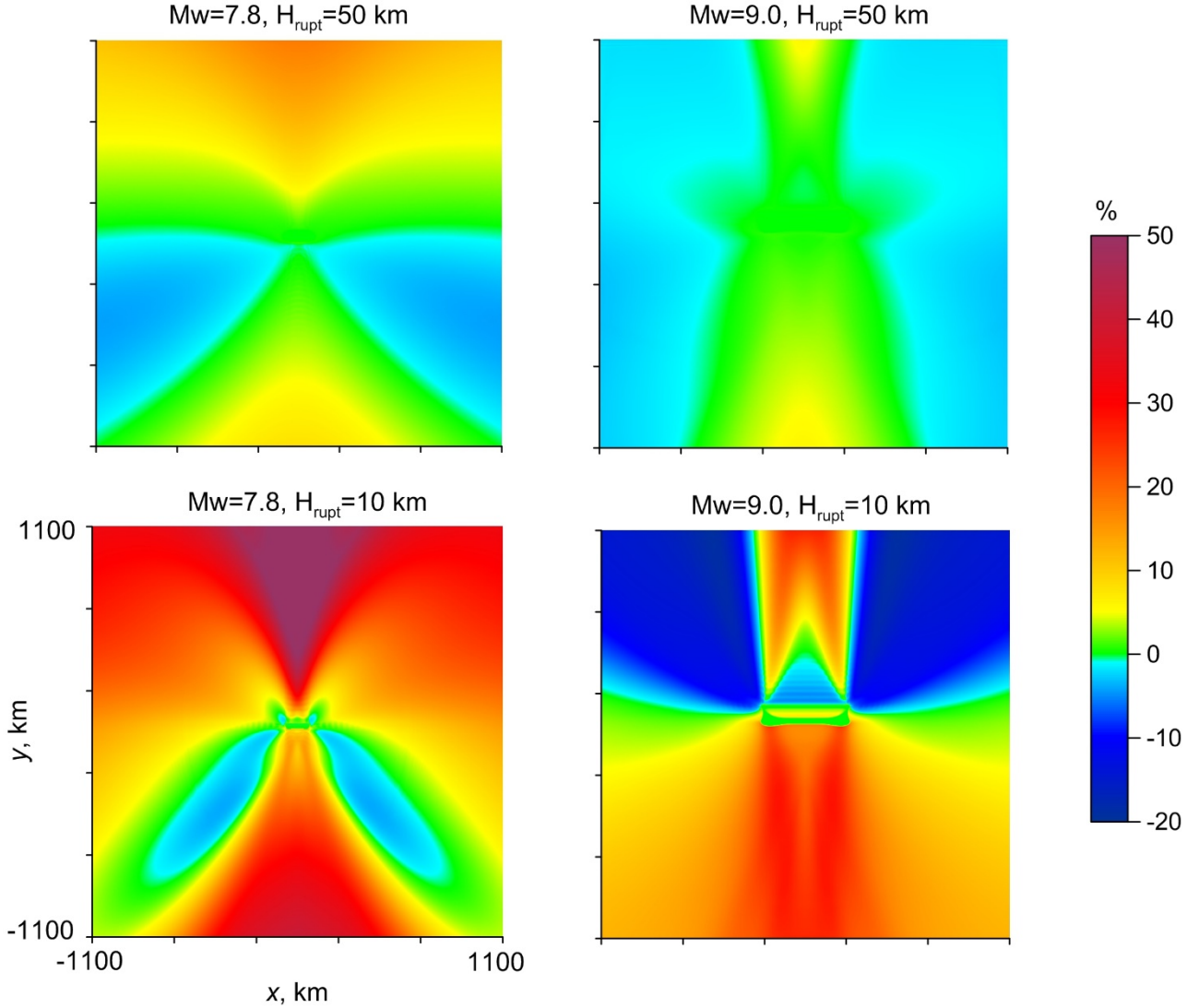

Figure 2. Relative differences in maximum surface elevation computed with FNLD and NLSW models for flat bottom test

Here we show the relative differences ((NLSW-FNLD)/NLSW) in the maximum surface elevation computed with the FNLD and the NLSW models. As one would expect, the lowest dispersion effects are observed in the case with $Mw = 9.0$ and $H_{rupt} = 50$ km, and the highest are observed in the case with $Mw = 7.8$ and $H_{rupt} = 10$ km. Increase of the magnitude leads to the increase of the effective extent of the initial wave profile, and decrease of the rupture depth makes the profile steeper. Surprisingly, the simulations show that the waves in the case with $Mw = 7.8$ and $H_{rupt} = 50$ km are much less affected by dispersion than the ones with $Mw = 9.0$ and $H_{rupt} = 10$ km. It means that the determinative factor for the dispersion effects is not an effective extent of the initial disturbance, but its form.

Nonlinear dispersive models are known to be inaccurate in simulations of moderate and short waves compared to water depth (see, for example, simulations of the landslide-generated tsunamis in Gusev et al. 2013; Gusev 2014; Lynett and Liu 2002). Considering the Okada source, it is difficult to estimate the characteristic wavelength. To check the adequacy of the FNLD model in the presented tests we consider transection $x = 0$ of the most dispersive case with $Mw = 7.8$ and $H_{rupt} = 10$ km (Fig. 3a), and perform the one-dimensional computations by the FNLD model and potential flow (PF) model (Khakimzyanov et al. 2001) which has no limitations on the wavelength. The comparisons of the computed surface profiles at time $t = 4800$ s are shown in Fig. 3b. We observe a very good agreement between the models, which proves the accuracy of the FNLD model in this class of tsunami problems.

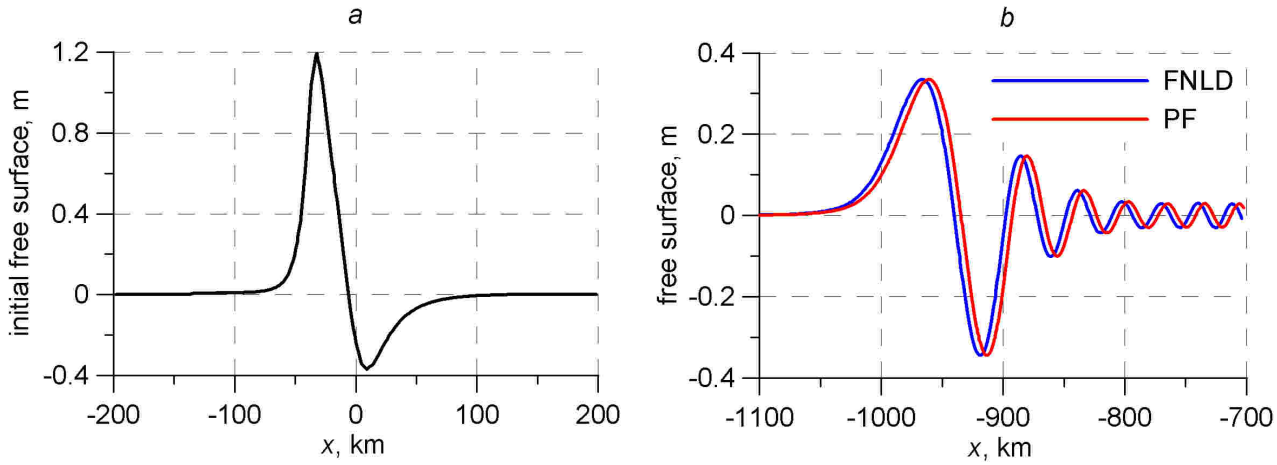

Figure 3. (*a*) Transection $x = 0$ of initial disturbance for the case with $Mw = 7.8$ and $H_{rupt} = 10$ km. (*b*) Parts of free surface profiles at time $t = 4800$ s computed by FNLD and PF models

2.4. Propagation in the "Wash-tube" domain

In this subsection, we investigate the sensitivity of the dispersion influence to the variation of some parameters in the Okada model of seismic source. For the computations the "Wash-tube" domain is employed (in Cartesian coordinates), in which the bottom function $\overline{h}$ is uniform in Ox direction, and in Oy direction it approximates the depth distribution of the Kuril-Kamchatka Trench (Fig. 4*a*).

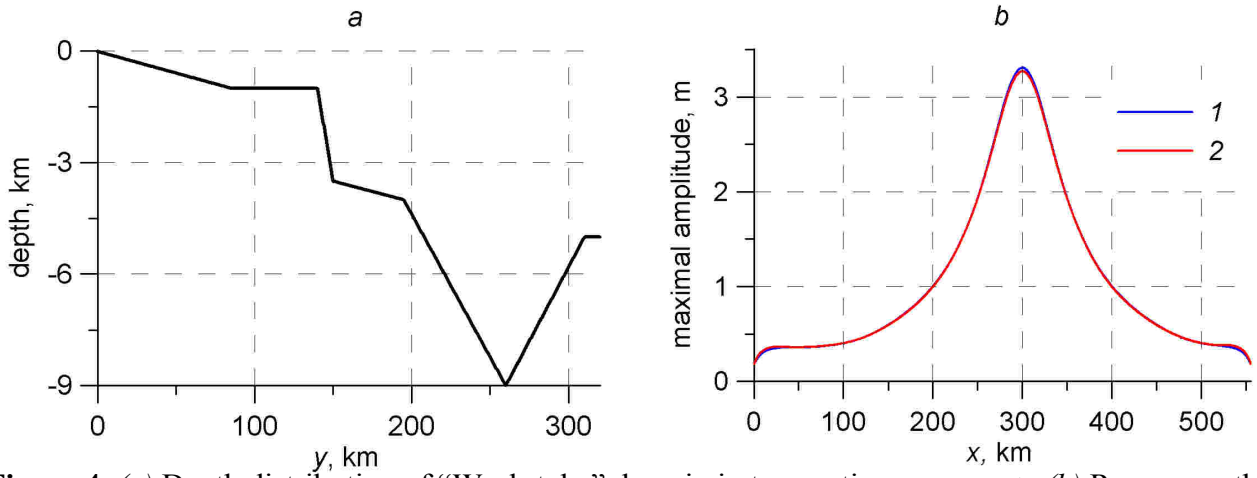

Figure 4. *(a)* Depth distribution of "Wash-tube" domain in transection $x = const$. *(b)* Run-up on the wall in the computations with the present FNLD model *(1)* and FUNWAVE *(2),* the source parameters are presented in (6)

Such basins were used (Chubarov and Gusiakov 1985) for nearfield tsunami investigations for the Russian coast of the Pacific Ocean. On the boundary $y = 0$, the vertical wall is mounted to simulate a wave run-up on the slope, the other boundaries are free. The depth value near the wall is 20 m. The horizontal size of the domain is specified by the parameters: $Lx_1 = Ly_1 = 0$, $Lx_2 = 555$ km, $Ly_2 = 320$ km. The computations are performed on the uniform grid with resolution $\Delta x = \Delta y = 125$ m, or with resolution $\Delta x = \Delta y = 62.5$ m for some NLSW model computations (Glimsdal et al. 2013, for example, noted that NLSW model solutions converge with grid refinement more slowly than NLD ones). The seismic sources are located near the center of the domain. Wave propagation time is set to two hours. Below, we estimate the dispersion influence through the comparisons of the maximal run-up distributions on the vertical wall.

We first consider sources with magnitude $Mw = 7.8$. With this magnitude, the following parameters are assumed to be fixed:

$L = 108$ km, $W = 38$ km, $D_0 = 2.9$ m.

To verify our two-dimensional code in this class of problems we make the comparison of obtained numerical solution of the FNLD model with the one of fully nonlinear model FUNWAVE (https://www.udel.edu/kirby/programs/funwave/funwave.html, Shi et al. 2012). The source parameters have the values

$$\theta_s = 270^o,\ \lambda_r = 90^o,\ \delta = 20^o,\ H_{rupt} = 10 \text{ km}. \quad (6)$$

The results of the comparison of the computed run-ups on the wall are presented in Fig. 4*b*. The excellent agreement between the models is observed. Note that the FUNWAVE computations were performed on a grid with resolution $\Delta x = \Delta y = 250$ m, that two times coarser than the grid in FNLD model computations. Nevertheless, the computation time (on a single CPU) and the size of the used memory were similar. For other verifications of the FNLD model in two-dimensional case, see (Gusev 2014).

2.4.1. Rupture depth variation

The first set of the computations is devoted to the variation of rupture depth from $H_{rupt} = 10$ km to $H_{rupt} = 50$ km with a step equal to 5 km. The other parameters of the sources are put as follows:

$$\theta_s = 270^o,\ \lambda_r = 90^o,\ \delta = 20^o.$$

The features of initial free surfaces and the obtained results are shown in Fig. 5. Here and below we illustrate the cross-sections $x = 300$ km of the initial surface elevations on the upper graph, obtained run-ups on the lowest one and corresponding absolute (NLSW-FNLD) and relative ((NLSW-FNLD)/NLSW) differences in the middle part of the figure. In this case, Fig. 5 clearly shows that the decrease of H_{rupt} significantly increases the maximal run-ups on the wall and the influence of dispersion. The reason is higher and steeper profile of the initial surface elevation. The absolute differences reach values up to 0.45 m while the relative ones amount up to 13 %. The relative differences may behave intricately near the bounds ($x = 0$ and $x = 555$ km) where the run-ups are small, so we cut the corresponding graphs at some distance from these bounds.

2.4.2. Dip-angle variation

For the computations with variation of δ we consider two cases of the strike-angle: $\theta_s = 270^o$ and $\theta_s = 90^o$. The dip-angle is changed from $\delta = 0^o$ to $\delta = 90^o$ with a step equal to 10^o.The rake angle is fixed, $\lambda_r = 90^o$, while the rupture depth is varied from $H_{rupt} = 11$ km to $H_{rupt} = 30$ km for the conservation of the position of the lower bound of the fault.

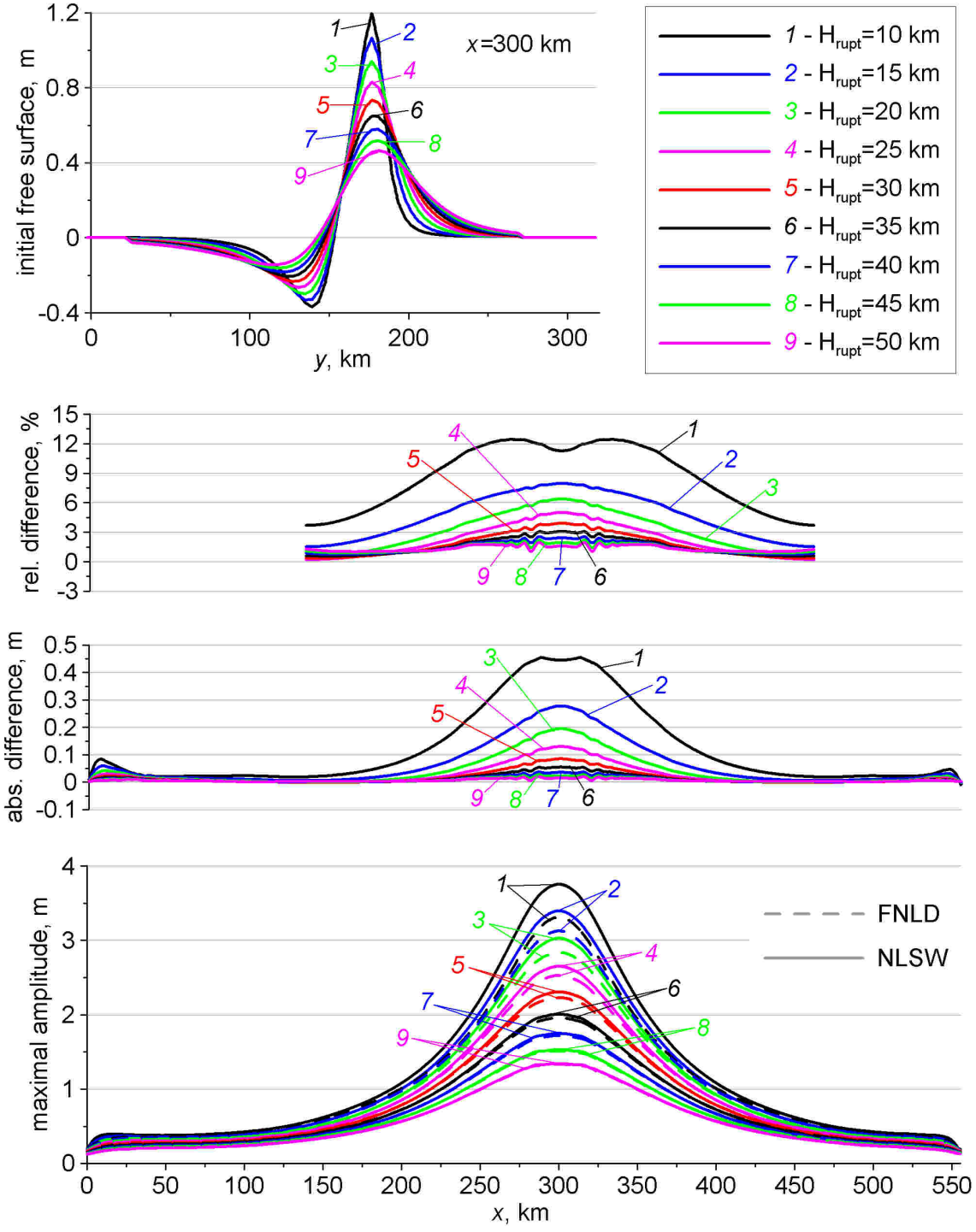

Figure 5. Dispersion effects sensitivity to rupture depth variation of the source with magnitude $Mw = 7.8$.

Fig. 6 illustrates the results of the computations with $\theta_s = 270^o$. It shows that the maximal run-ups is fixed with the minimal dip-angle, $\delta = 0^o$, despite the fact that initial free surface was not

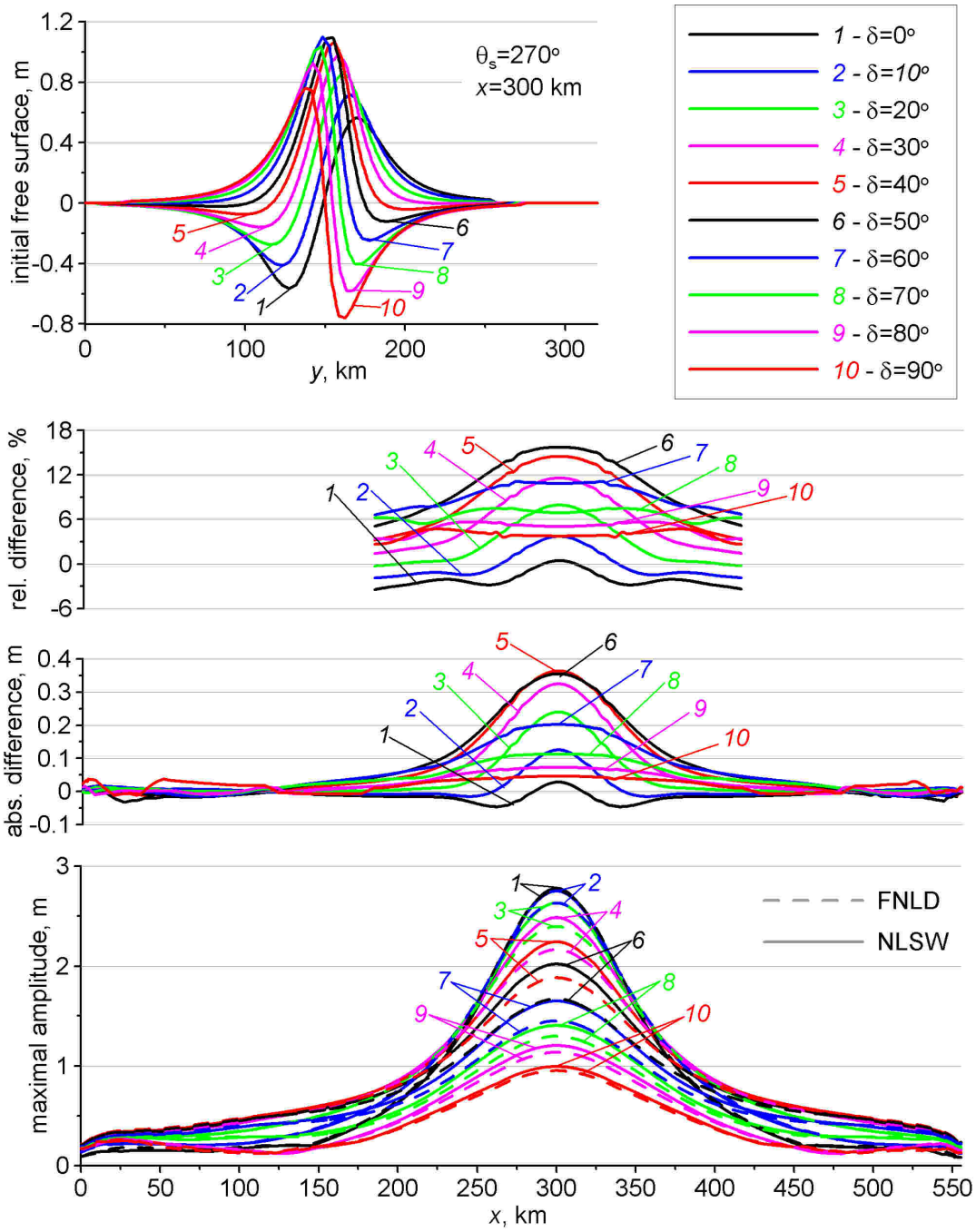

Figure 6. Dispersion effects sensitivity to dip-angle variation of the source with magnitude $Mw = 7.8$. Case with $\theta_s = 270^o$

the highest in this case. Such effect is associated with the depression wave arrived at the wall before the main positive one (see, for example, Tadepalli and Synolakis 1994; Didenkulova et al. 2014). Vice versa, with $\delta = 90^o$ the depression wave arrived after the main positive one and the run-ups are minimal. The maximal dispersion effects are observed in the cases with $\delta = 40^o$ and $\delta = 50^o$, when the initial free surfaces are the highest. The absolute differences are up to 0.35 m while the relative ones are up to 16%.

Changing the strike-angle to $\theta_s = 90^o$ rotates the initial free surfaces 180 degrees in the horizontal plane. The obtained results (Fig. 7) have some differences from the previous set of experiments. Again, the sources with the depression part located farther from the wall than the positive elevation ($\delta \le 40^o$) generate lower run-ups which are less affected by dispersion. The increase of the dip-angle ($\delta \ge 50^o$) increases the run-ups, but the dispersion influence is not trivial in these cases. Fig. 7 shows that the differences in the NLSW and the FNLD computations become negative at approximately 50 km far from the abscissa of the run-up maximum, meaning that the dispersion effects increase the wave height there. Regard to the absolute differences, the maximal one (≈ 0.45 m) is obtained with $\delta = 80^o$ while the minimum one (≈ -0.13 m) corresponds to $\delta = 90^o$. Maximal relative differences ($\approx 10\%$) are observed with $\delta = 60^o$, $\delta = 70^o$ and $\delta = 80^o$, the minimal one ($\approx -14\%$) is computed with $\delta = 90^o$.

2.4.3. Rake-angle variation

The rake-angle is changed from $\lambda_r = 0^o$ to $\lambda_r = 90^o$ with a step equal to 10^o. The other parameters are assigned as follows:

$H_{rupt} = 10$ km, $\delta = 20^o$, $\theta_s = 270^o$.

Fig. 8 shows the results of the computations. At the upper panel of the figure, we bring the main fragments of the initial free surface elevations for clearer comparisons. The computations show that the variation of the rake-angle has a strong influence on the run-up, increasing it with the increase of λ_r. The absolute differences in the NLSW and the FNLD behave similarly and reach ≈ 0.44 m.

However, the relative differences have the inverse behavior, tending to decrease it values with increase of λ_r. The maximal relative differences are observed far from the center of the wall where the run-ups are small.

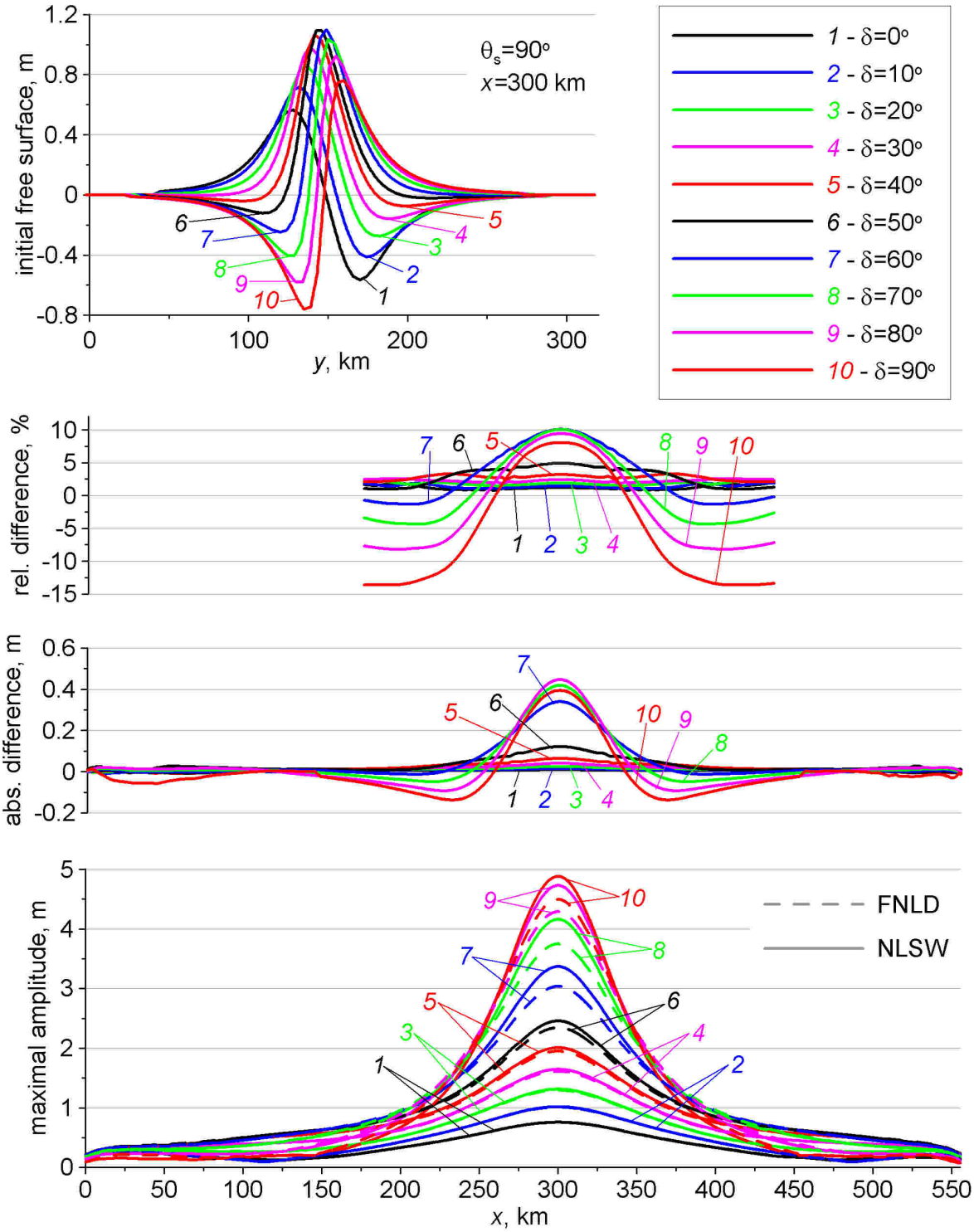

Figure 7. Dispersion effects sensitivity to dip-angle variation of the source with magnitude $Mw = 7.8$. Case with $\theta_s = 90^o$

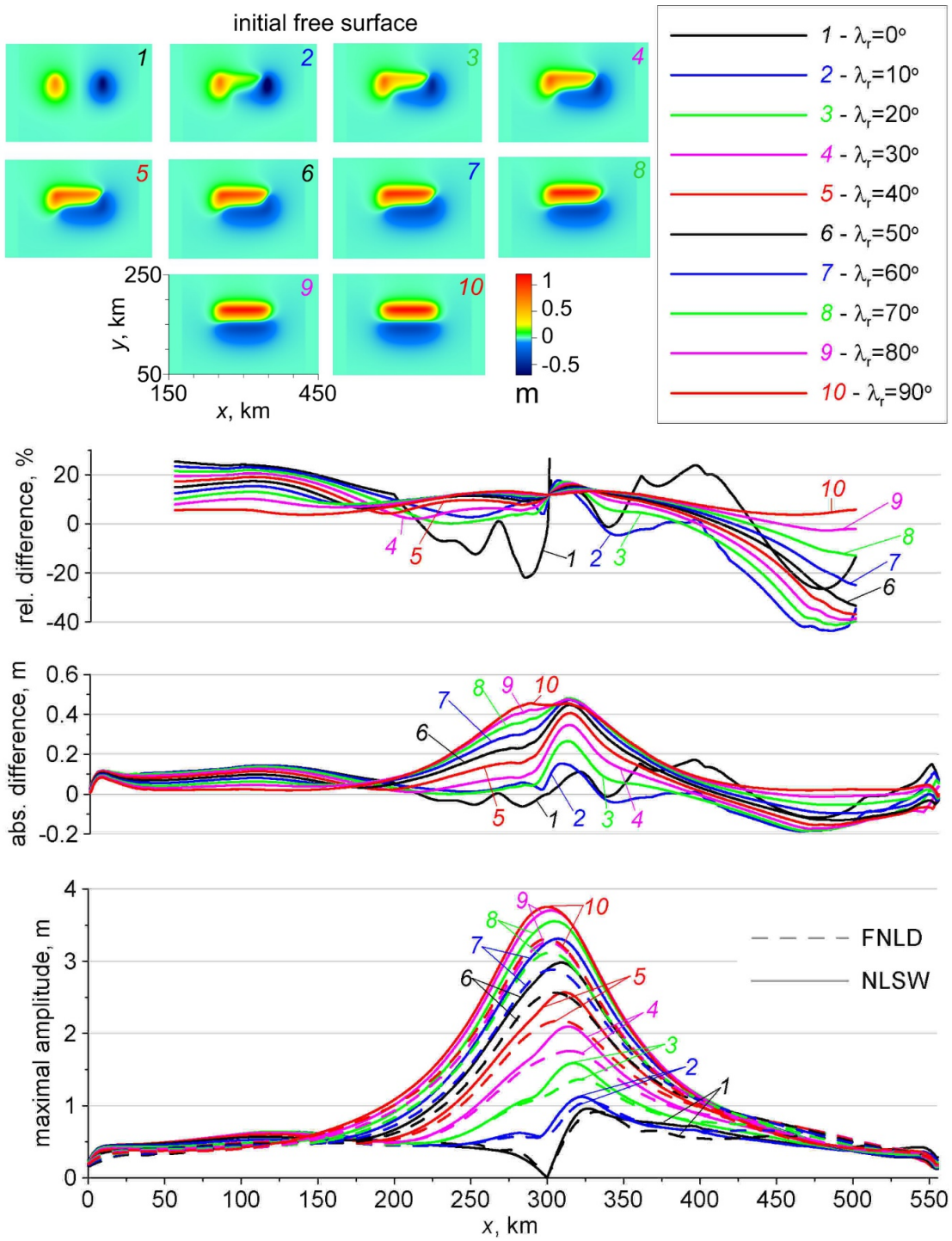

Figure 8. Dispersion effects sensitivity to rake-angle variation of the source with magnitude $Mw = 7.8$

2.4.4. Rupture depth variation for source with $Mw = 9.0$

Finally, we demonstrate how the dispersion sensitivity to the rupture depth of the source can be changed with consideration of the source with magnitude $Mw = 9.0$. For this case, the following characteristic parameters are chosen:

$$L = 430 \text{ km}, \; W = 150 \text{ km}, \; D_0 = 11.6 \text{ m}.$$

All other parameters of the sources are the same as in item 3.2.1. The results of the computations are presented in Fig. 9. Analyzing the maximal run-ups on the wall one can note that decreasing of the rupture depth from $H_{rupt} = 50$ km to $H_{rupt} = 30$ km leads to the increase of the run-ups in both FNLD and NLSW computations. With further decrease of H_{rupt} the run-up in the NLSW computations increase while in the FNLD ones decrease. For the minimal value, $H_{rupt} = 10$ km, the absolute difference between this computations reaches ≈ 3.5 m, and the relative one amounts $\approx 32\%$. Comparisons of the results of these experiments with those in item 3.2.1 show that the dispersive effects of waves generated by earthquakes with larger magnitude may be even more sensitive to the variation of the source parameters.

Note that the simulations in this section are carried out in the model basin for nearfield tsunamis. Considering a far-field propagation, one should expect a significant increase of the dispersion influence. Our computations provide the qualitative results on the importance of source parameters on the dispersion effects.

2.5. Potential tsunami on a real bathymetry

In this subsection, we simulate the propagation of the tsunami generated by potential seismic source near Papua New Guinea. The parameters of the source have the following values:

$$L = 430 \text{ km}, \; W = 150 \text{ km}, \; \delta = 45^o, \; \lambda_r = 90^o, \; \theta_s = 50^o, \; D_0 = 11.6 \text{ m}, \; H_{rupt} = 10 \text{ km}.$$

The FNLD and the NLSW computations were performed on a GEBCO 1-minute grid. The computational domain lies in latitude direction from $12S$ to $63N$ and in longitude one from $127E$ to $173W$. The wave propagation time is set to 12 hours.

We first consider a case with the idealized bathymetry ($\bar{h} \equiv 4$ km) and then a real one. Thus, the simulations allow estimating the influence of the bottom irregularities on the maximal amplitude distribution and on the dispersion effects. Fig. 10 illustrates that this influence appears to be strong.

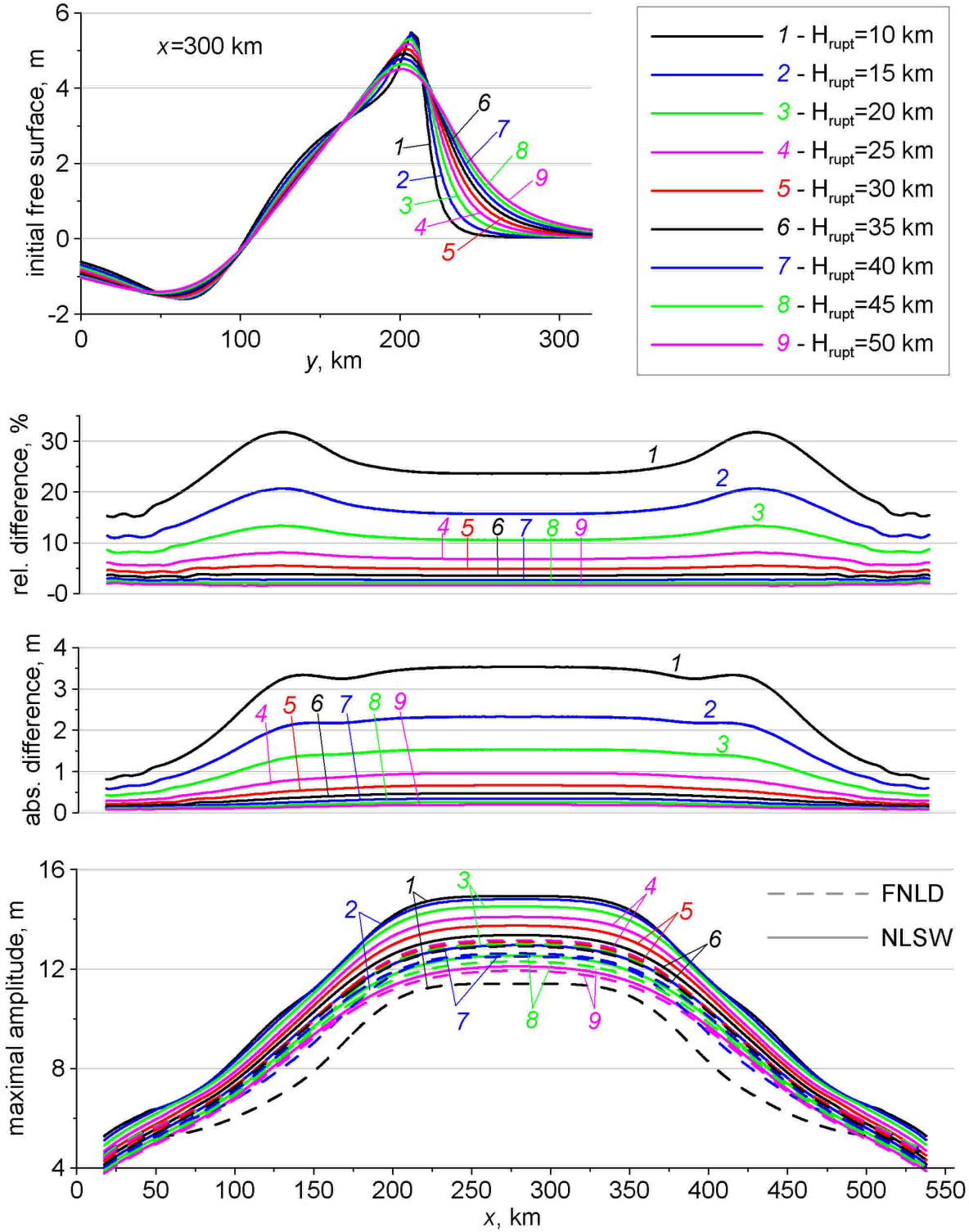

Figure 9. Dispersion effects sensitivity to rupture depth variation of the source with magnitude $Mw = 9.0$

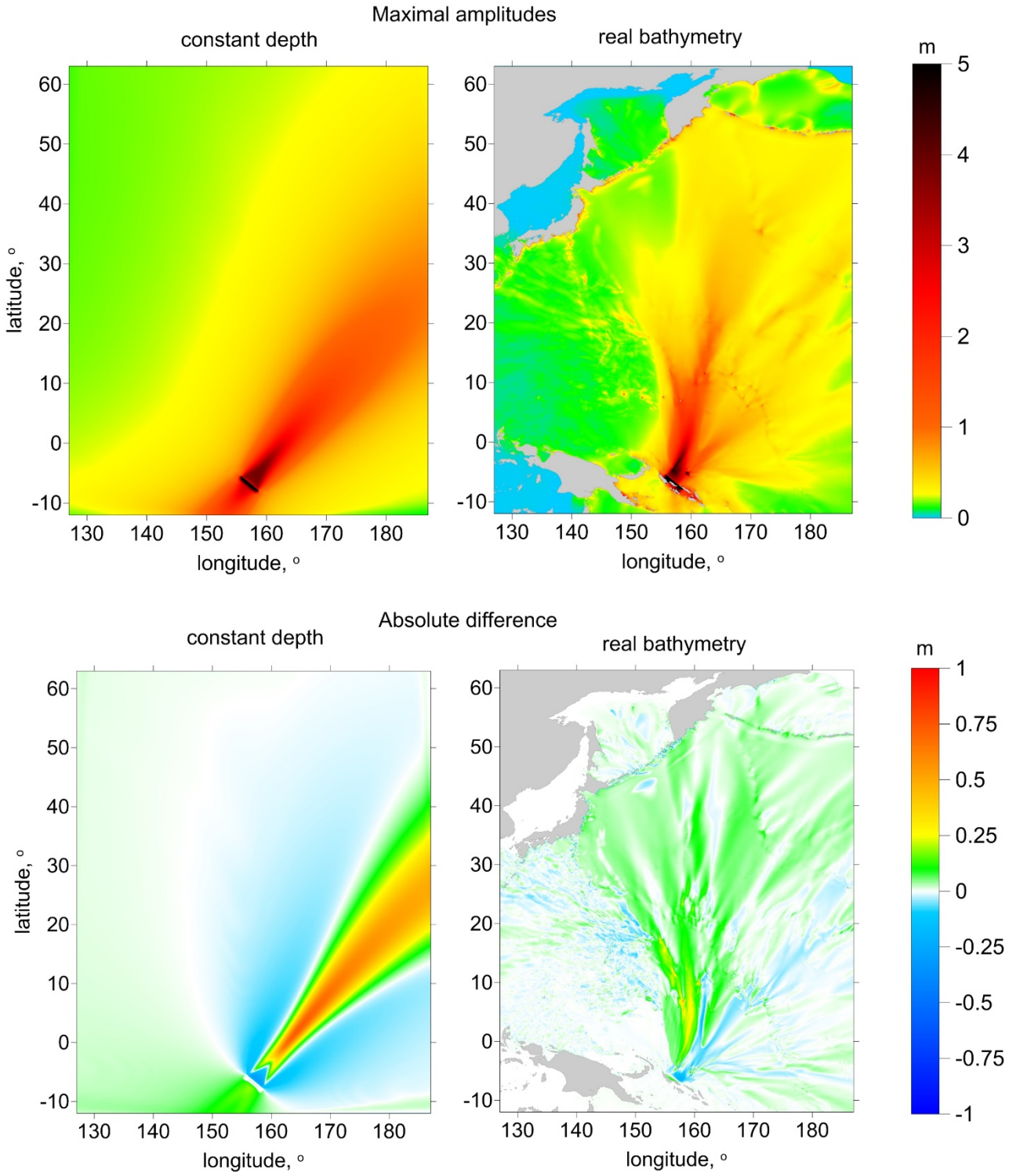

Figure 10. Maximal amplitudes (upper panel) calculated with FNLD model and absolute differences between NLSW and FNLD computations (lower panel) for the potential tsunami source near Papua New Guinea on the idealized and the real bathymetry

The bottom irregularities change the direction of the maximal amplitudes and significantly complicate its pattern. The dispersion effects are generally smaller on the real bathymetry where behave complicatedly. Such behavior was observed, for example, in study (Kirby et al. 2013) during the simulation of Tohoku tsunami with using of a weakly nonlinear dispersive model. It seems that details of the bottom impact on the dispersion effects are still unclear and require further investigations. In our future work, we will consider several bottom configurations with idealized irregularities to investigate this impact.

3. CONCLUSION

In this study, we have investigated the influence of seismic source parameters on the frequency dispersion effects. These effects were estimated through the comparisons between the computations with a fully nonlinear dispersive model on a rotating sphere and with a nondispersive shallow water model. In general, the obtained results show a strong sensitivity of the dispersion effects to a rupture depth and to a dip-angle of a source. The main reason is the presence of the high frequency components in the initial surface disturbance. Counterintuitively, waves generated by sources with lager magnitude may be even more affected by dispersion. Consequently, the main factor for the dispersion manifestation is the form of the initial disturbance, but not the source extensions. Bottom irregularities may also have a significant impact on a display of dispersion. This impact will be the subject of our future investigations.

4. ACKNOWLEDGEMENTS

This research was supported by RSCF project No 14-17-00219. The authors would like to thank Gayaz Salimovich Khakimzyanov (ICT SB RAS), Leonid Borisovich Chubarov (ICT SB RAS) and Vyacheslav Konstantinovich Gusiakov (ICMMG SB RAS, ICT SB RAS) for their valuable comments on the manuscript.

REFERENCES

Cherevko A.A. and Chupakhin A.P. (2009). Equations of the shallow water model on a rotating attracting sphere.1. Derivation and general properties. J. Appl. Mech. Tech. Phys. Vol. 50, No 2. P 188–198.

Chubarov L.B. and Guslakov V.K. (1985). Tsunamis and earthquake mechanisms in the island arc regions // Science of Tsunami Hazards. Tsunami Society, Honolulu, USA. Vol. 3, No 1. P. 3–21.

Dao M.H. and Tkalich P. (2007). Tsunami propagation modelling — a sensitivity study. Nat. Hazards Earth Syst. Sci. Vol. 7. P. 741–754.

Didenkulova I.I., Pelinovsky E.N. and Didenkulov O.I. (2014). Run-up of long solitary waves of different polarities on a plane beach. Izv. Atmos. Oceanic Phys. Pleiades Publishing. Vol. 50, No 5. 532–538.

Fedotova Z.I. and Khakimzyanov G.S. (2010). Nonlinear-dispersive shallow water equations on a rotating sphere. Russian Journal of Numerical Analysis and Mathematical Modelling. De Gruyter. Vol. 25, No 1. P. 15–26.

Fedotova Z.I. and Khakimzyanov G.S. (2014). Nonlinear-dispersive shallow water equations on a rotating sphere and conservation laws. Journal of Applied Mechanics and Technical Physics. Springer. Vol. 55, No 3. P. 404–416.

Fedotova Z.I., Khakimzyanov G.S. and Gusev O.I. (2015). History of the development and analysis of numerical methods for solving nonlinear dispersive equations of hydrodynamics. I. One-dimensional models problems. Computational Technologies. Russia, ICT SB RAS. Vol. 20, No 5. P. 120–156 (In Russian).

Glimsdal, S., Pedersen G.K., Harbitz C.B. and Lovholt F. (2013). Dispersion of tsunamis: does it really matter? Nat. Hazards Earth Syst. Sci. Vol. 13. P. 1507–1526.

Gusev O.I. (2012). On an algorithm for surface waves calculation within the framework of nonlinear dispersive model with a movable bottom. Computational technologies. Russia, ICT SB RAS. Vol. 17, No. 5. P. 46–64 (In Russian).

Gusev O.I. (2014). Algorithm for surface waves calculation above a movable bottom within the frame of plane nonlinear dispersive model. Computational technologies. Russia, ICT SB RAS. Vol. 19, No 6. P. 19–41 (In Russian).

Gusev O.I. and Khakimzyanov G.S. (2015). Numerical simulation of long surface waves on a rotating sphere within the framework of the full nonlinear dispersive model. Computational Technologies. Russia, ICT SB RAS. Vol. 20, No 3. P. 3–32 (In Russian).

Gusev O.I., Shokina N.Y., Kutergin V.A. and Khakimzyanov G.S. (2013). Numerical modelling of surface waves generated by underwater landslide in a reservoir. Computational technologies. Russia, ICT SB RAS. Vol. 18, No 5. P. 74–90 (In Russian).

Gusiakov V.K. (1978). Static displacement on the surface of an elastic space. Ill-posed problems of mathematical physics and interpretation of geophysical data. Novosibirsk, VC SOAN SSSR. P. 23–51 (in Russian).

Horrillo J., Grilli S.T., Nicolsky D., Roeber V., Zhang J. (2015). Performance benchmarking tsunami models for NTHMP's inundation mapping activities. Pure Appl. Geophys. Vol. 172, No. 3–4. P. 869–884.

Kajiura K. (1963). The leading wave of a tsunami. Bull. Earthq. Res. Inst. Vol. 41. P. 535–571.

Khakimzyanov G.S., Gusev O.I., Beisel S.A., Chubarov L.B. and Shokina N.Yu. (2015). Simulation of tsunami waves generated by submarine landslides in the Black Sea. Russian Journal of Numerical Analysis and Mathematical Modelling. De Gruyter. Vol. 30, No 4. P. 227–237.

Khakimzyanov G.S., Shokin Yu.I., Barakhnin V.B. and Shokina N.Yu. (2001). Numerical modelling of fluid flows with surface waves. Publishing House of SB RAS, Novosibirsk (In Russian).

Kirby J.T., Shi F., Tehranirad B., Harris J.C. and Grilli S.T. (2013). Dispersive tsunami waves in the ocean: Model equations and sensitivity to dispersion and Coriolis effects. Ocean Modelling. Vol. 62. P. 39–55.

Kosykh V.S., Chubarov L.B., Gusiakov V.K., Kamaev D.A., Grigor'eva V.M. and Beisel S.A. (2013). A technique for computing maximum heights of tsunami waves at protected Far Eastern coastal points of the Russian Federation. Results from Testing of New and Improved Technologies, Models, and Methods of Hydrometeorological Forecasts. IG SOTsIN, Moscow–Obninsk. No 40, P. 115–134 (In Russian).

Lovholt F., Pedersen G.K. and Gisler G. (2008). Oceanic propagation of a potential tsunami from the La Palma Island. J. Geophys. Res. Vol. 113. C09026.

Lynett P.J. and Liu P.L.-F. (2002). A numerical study of submarine-landslide-generated waves and run-up. Proc. Royal Society of London. A. Vol. 458. P. 2885–2910.

Okada Y. (1985). Surface deformation due to shear and tensile faults in a half space. Bull. Seism. Soc. Am. Vol. 75. P. 1135–1154.

Pelinovsky E.N. (1996). Hydrodynamics of tsunami waves. Institute of Applied Physics RAS, Nizhny Novgorod (In Russian).

Shi F, Kirby J.T., Harris J.C., Geiman J.D., Grilli S.T. (2012). A high-order adaptive time-stepping TVD solver for Boussinesq modeling of breaking waves and coastal inundation. Ocean Modelling. Vol. 43–44. P. 36–51.

Shokin Yu.I., Babailov V.V., Beisel S.A., Chubarov L.B., Eletsky S.V., Fedotova Z.I., Gusiakov V.K. (2008). Mathematical Modeling in Application to Regional Tsunami Warning Systems Operations. Notes on Numerical Fluid Mechanics and Multidisciplinary Design. Berlin: Springer. Vol. 101: Computational Science and High Performance Computing III. P.52–68.

Tadepalli S. and Synolakis C.E. (1994). The runup of N-waves. Proc. Royal Soc. London. A445. P. 99–112.

Titov V. and Synolakis , C.E. (1995). Evolution and runup of breaking and nonbreaking waves using VTSC2. Journal of Waterway, Port, Coastal and Ocean Engineering. Vol. 126, No 6. P. 308–316.

ISSN 8755-6839

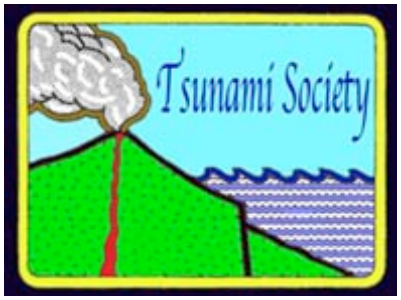

SCIENCE OF **TSUNAMI HAZARDS**

Journal of Tsunami Society International

Volume 35 **Number 2** **2016**

TSUNAMI SOCIETY INTERNATIONAL, 1741 Ala Moana Blvd. #70, Honolulu, HI 96815, USA.

WWW.TSUNAMISOCIETY.ORG